

1 **Implementation and assessment of a carbonate system model**
2 **(Eco3M-CarbOx v1.1) in a highly-dynamic Mediterranean**
3 **coastal site (Bay of Marseille, France).**

4 Katixa Lajaunie-Salla¹, Frédéric Diaz¹, Cathy Wimart-Rousseau¹, Thibaut Wagener¹, Dominique
5 Lefèvre¹, Christophe Yohia², Irène Xueref-Remy³, Brian Nathan³, Alexandre Armengaud⁴,
6 Christel Pinazo¹

7 ¹Aix Marseille Univ., Université de Toulon, CNRS, IRD, MIO, UM 110, 13288, Marseille, France

8 ²Aix Marseille Univ., CNRS, IRD, OSU Institut Pythéas, 13288, Marseille, France

9
10 ³Aix Marseille Univ., Université d'Avignon, CNRS, IRD, IMBE, Marseille, France

11 ⁴AtmoSud : Observatoire de la qualité de l'air en région Sud Provence Alpes Côte d'Azur, le Noilly Paradis, 146 rue
12 Paradis, 13294 Marseille, Cedex 06, France

13

14 *Correspondance to* : Katixa Lajaunie-Salla (katixa.lajaunie@gmail.com), Frédéric Diaz (frederic.diaz@univ-amu.fr)

15 **Abstract.** A carbonate chemistry balance module was implemented into a biogeochemical model of the planktonic
16 food web. The model, named Eco3M-CarbOx includes 22 state variables that are dispatched into 5 compartments:
17 phytoplankton, heterotrophic bacteria, detrital particulate organic matter, labile dissolved organic and inorganic matter.
18 This model is applied to and evaluated in the Bay of Marseille (BoM, France) that is a coastal zone impacted by the
19 urbanized and industrialized Aix-Marseille Metropolis, and subject to significant increases in anthropogenic emissions
20 of CO₂.

21 The model was evaluated over the year 2017 for which *in situ* data of carbonate system are available in the study site.
22 The biogeochemical state variables of the model only change with time, to represent the time evolution of a sea surface
23 water cell in response to the implemented realistic forcing conditions. The model correctly simulates the values ranges
24 and seasonal dynamics of most of variables of carbonate system except for the total alkalinity. Several numerical
25 experiments were conducted to test the response of carbonate system to (i) a seawater temperature increase, (ii) wind
26 events, (iii) Rhône River plume intrusions and (iv) levels of atmospheric CO₂ contents. This set of numerical
27 experiments shows that the Eco3M-CarbOx model provides expected responses in the alteration of the marine
28 carbonate balance regarding each of the considered perturbation. When the seawater temperature changes quickly, the
29 behaviour of the BoM waters alters within a few days from a source of CO₂ to the atmosphere to a sink into the ocean.
30 Moreover, the higher the wind speed is, the higher the air-sea CO₂ gas exchange fluxes are. The river intrusions with
31 nitrate supplies lead to a decrease in the *p*CO₂ value, favouring the conditions of a sink for atmospheric CO₂ into the
32 BoM. A scenario of high atmospheric concentrations of CO₂ also favours the conditions of a sink for atmospheric CO₂
33 into the waters of the BoM. Thus the model results suggest that external forcings have an important impact on the
34 carbonate equilibrium in this coastal area.

35

36 1. Introduction

37 Current climate change mostly originates from the carbon dioxide (CO₂) increase in the atmosphere at a high annual
38 rate (+2.63 ppm from May 2018 to May 2019, <https://www.esrl.noaa.gov/gmd/ccgg/trends/global.html>). This
39 atmospheric CO₂ increase impacts the carbonate chemistry equilibrium of the oceanic water column (Allen et al., 2009;
40 Matthews et al., 2009). Oceans are known to act as a sink for anthropogenic CO₂, *i.e.* 30% of emissions, which leads
41 to a marine acidification (Gruber et al., 2019; Orr et al., 2005; Le Quéré et al., 2018).

42 CO₂ is a key molecule in the biogeochemical functioning of the marine ecosystem. Photo-autotrophic organisms,
43 mainly phytoplankton and macro-algae, fix this gas through photosynthesis in the euphotic zone and, in turn, produce
44 organic matter and dissolved oxygen. Heterotrophic organisms, mainly heterotrophic protists and metazoans consume
45 organic matter and dissolved oxygen by aerobic respiration and, in turn, produce CO₂. In the Ocean, the main processes
46 regulating CO₂ exchanges between the atmosphere and sea are the solubility pump and the biological pump at different
47 time-scales. Overall, the thermohaline gradients drive the solubility pump, while the metabolic processes of gross
48 primary production and respiration set the intensity of the biological pump (Raven and Falkowski, 1999).

49 The coastal zones, despite their small surface area and volume compared to those of the open ocean, have a large
50 influence upon carbon dynamics and represent 14 to 30% of the oceanic primary production (Gattuso et al., 1998). At
51 the interface between open-ocean and continents, these zones receive large inputs of nutrients and organic matter from
52 rivers, groundwater discharge, and from atmospheric depositions (Cloern et al., 2014; Gattuso et al., 1998). On coasts,
53 shorelines are subject to an increasing density of population and associated urbanization (Small and Nicholls, 2003).
54 This rapid alteration of shorelines all over the world accelerates the emissions of greenhouses gases near the coastal
55 ocean, and it also involves large discharges of material into the seawater by wastewater runoff and/or rivers (Cloern,
56 2001). These anthropogenic forcing alter the biogeochemical functioning of these zones and could lead to a growing
57 eutrophication (Cloern, 2001). Moreover, these forcing could affect the carbonate chemistry dynamics and amplify or
58 attenuate the acidification in coastal zones. This alteration of the marine environment may provoke further changes in
59 the structure of the plankton community, including *in fine* consequences on the populations with high trophic levels,
60 such as teleosts (Esbaugh et al., 2012). At the global scale, coastal zones are considered to be a significant sink for
61 atmospheric CO₂, with an estimated flux converging to 0.2 PgC y⁻¹ (Roobaert et al., 2019). However, some studies
62 highlight that the status of these areas as a net sink or source still remains uncertain due to the complexity of the
63 interactions between biological and physical processes, and also due to the lack of *in situ* measurements (Borges and
64 Abril, 2011; Chen et al., 2013; Chen and Borges, 2009). Moreover, the capacity for coastal zones to absorb atmospheric
65 CO₂ resulting from the increasing human pressure also remains poorly known. There are few works which highlight,
66 under future atmospheric CO₂ levels, whether coastal zones will become a net sink or a reduced source of CO₂
67 (Andersson and Mackenzie, 2012; Cai, 2011).

68 The current increase in the atmospheric CO₂ partial pressure (*p*CO₂) is slowly shifting the marine carbonate chemistry
69 equilibrium towards increases in the seawater *p*CO₂ and bicarbonate ions (HCO₃⁻) and decreases in *p*H and carbonate
70 ions (CO₃²⁻) (Hoegh-Guldberg et al., 2018). These trends were already described in several coastal and open-ocean
71 locations worldwide (Cai et al., 2011). In a coastal Northwestern Mediterranean site, a 10-year time-series of *in situ*
72 measurements highlights a trend of *p*H decrease and *p*CO₂ increase (Kapsenberg et al., 2017). Low *p*H values can
73 inhibit the ability of many marine organisms to form the calcium carbonate (CaCO₃) used in the making of skeletons
74 and shells (Gattuso et al., 2015). In an extreme case, this shift may promote dissolution of CaCO₃ because the water
75 will become under-saturated with respect to CaCO₃ minerals (Doney et al., 2009).

76 The present study is dedicated to the implementation of a carbonate system module into a preexisting biogeochemical
77 model of planktonic food web. This new model, named Eco3M-CarbOx (v1.1) is then evaluated in a highly-dynamic

78 coastal site, *i.e.* Bay of Marseille (BoM) in the Northwestern Mediterranean Sea. This evaluation is performed on the
79 seasonal dynamics of biogeochemical and carbonate modeled variables against that of the corresponding *in situ* data
80 available over the year 2017. This study is extended by a fine analysis of the variability of the marine carbonate system
81 (stocks, fluxes) in relation to physical (*e.g.* wind events, river intrusions, temperature increases, changes in the
82 atmospheric $p\text{CO}_2$ levels) and biogeochemical processes (gross primary production (GPP) and respiration (R)) in the
83 study site. The BoM is suitable to this kind of study because this coastal area is subject to high emissions of atmospheric
84 CO_2 from the nearby urban area, and it also receives effluents from the Aix-Marseille metropolis. In addition, strong
85 wind events (Mistral) regularly occur, which could lead to (i) strong latent heat losses at the surface (Herrmann et al.,
86 2011) and upwelling along the coast with a common consequence of cooling effect and (ii) Rhône River plume
87 intrusion under specific wind conditions (Frayse et al., 2013, 2014). In this regional context, many anthropogenic
88 forcing can interact with the dynamics of the carbonate systems. Natural determinants of the composition of the marine
89 planktonic community can also play a crucial role in these dynamics.

90 **2. Materials & Methods**

91 **2.1 Numerical model description**

92 The Eco3M-CarbOx biogeochemical model was developed to represent the dynamics of the seawater carbonate system
93 and plankton food web in the BoM. The model was implemented using the Eco3M (Ecological Mechanistic and
94 Modular Modelling) platform (Baklouti et al., 2006). The model structure used is based on an existing model of the
95 plankton ecosystem (Frayse et al., 2013), including a description of Carbon (C), Nitrogen (N) and Phosphorus (P)
96 marine biogeochemical cycles. The Eco3M-CarbOx model includes 22 prognostic state variables that are split into 5
97 compartments: phytoplankton, heterotrophic bacteria, detrital particulate organic matter, labile and semi-labile
98 dissolved organic matter, nutrients (ammonia, nitrate and phosphate), dissolved oxygen, and carbonate system
99 variables (Fig. 1). In this study, the state variables of the Eco3M-CarbOx model only change along time (*i.e.* usually
100 termed “model 0D”), they are representative of the time evolution of a sea surface water cell but this biogeochemical
101 model is not coupled with a hydrodynamic model.

102 The model presented in this study includes a set of new developments and improvements in the realism of the plankton
103 web structure and process formulations compared to the model of Frayse et al. (2013). In order to improve the
104 representation of chlorophyll concentration in the Bay of Marseille the phytoplankton is divided in two groups: one
105 with some ecological and physiological traits of the *Synechococcus* cyanobacteria, which is one of the major
106 constitutive members of pico-autotrophs in Mediterranean Sea (Mella-Flores et al., 2011), and another with traits of
107 large diatoms, which are generally observed during spring blooms at mid-latitudes (Margalef, 1978). For both of the
108 phytoplankton, there is a diagnostic chlorophyll-a variable related to the phytoplankton C-biomass, the phytoplankton
109 N-to-C ratio, and the limiting internal ratio f_Q^N (Faure et al., 2010; Smith and Tett, 2000; Tab. B2, Appendix B). The
110 functional response of primary production was modified using another formulation of temperature limitation function
111 which takes into account the optimal temperature of growth for each phytoplankton group. The exudation of
112 phytoplankton was modified taking into account the intracellular phytoplankton ratio. For the uptake of matter by
113 bacteria and the remineralization processes the dependence on intracellular bacteria ratio was modified. A temperature
114 dependence of all biogeochemical processes was added to take into account the effects of rapid and strong variations
115 of seawater temperature on plankton during episodes of upwelling for instance that are usually observed in the BoM.
116 Also certain parameters in some formulations were modified owing to the alterations of some formulations (Tabs. B4
117 & B5, Appendix B).

118 Additionally, a carbonate system module was developed and three state variables were added: dissolved inorganic
119 carbon (DIC), total alkalinity (TA) and the calcium carbonate (CaCO_3) implicitly representing calcifying organisms.
120 The knowledge of DIC and TA allows the calculation of the $p\text{CO}_2$ and $p\text{H}$ (total $p\text{H}$ scale) diagnostic variables,
121 necessary for resolving all the equations of the carbonate system. These equations use apparent equilibrium constants,
122 which depend on temperature, pressure, and salinity (Dickson, 1990a, 1990b; Dickson and Riley, 1979; Lueker et al.,
123 2000; Millero, 1995; Morris and Riley, 1966; Mucci, 1983; Riley, 1965; Riley and Tongudai, 1967; Uppström, 1974;
124 Weiss, 1974). The details of the resolution of carbonate system module are given in the Appendix A. For this module
125 three processes were also added: the precipitation and dissolution of calcium carbonate and the gas exchange of $p\text{CO}_2$
126 with the atmosphere. Based on the review of Middelburg (2019), it is considered that: (i) TA decreases by 2 moles for
127 each mole of CaCO_3 precipitated, by 1 mole for each mole of ammonium nitrified, by 1 mole for each mole of
128 ammonium assimilated by phytoplankton, and TA increases by 2 moles for each mole of CaCO_3 dissolved, and by 1
129 mole for each mole of organic matter mineralized by bacteria in ammonium (Tab. B2, Appendix B). (ii) DIC is
130 consumed during the photosynthesis and calcification processes and is produced by respiration (of phytoplankton,
131 zooplankton, and bacteria) and the CaCO_3 dissolution processes. Moreover, the dynamics of DIC are altered by the
132 CO_2 exchanges with the atmosphere (Tab. B2, Appendix B). The air-sea CO_2 fluxes are calculated from the $p\text{CO}_2$
133 gradient across the air-sea interface and the gas transfer velocity (Tab. B3, Appendix B) estimated from the wind speed
134 and using the parametrization of Wanninkhof (1992).
135 In the Eco3M-CarbOx model, zooplankton is considered as an implicit variable. However, a closure term based on the
136 assumption that all of the matter grazed by the zooplankton and higher trophic levels returns as either organic or
137 inorganic matter by excretion, egestion and mortality processes is taken into account (Frayse et al., 2013). The model
138 considers a “non-redfieldian” stoichiometry for phytoplankton and bacteria. All the biogeochemical model
139 formulations, equations and associated parameters values are detailed in the Appendix B.

140 2.2 Study area

141 The BoM is located in the eastern part of the Gulf of Lions, in the Northwestern Mediterranean Sea (Fig. 2). The city
142 of Marseille, located on the coast of the BoM, is the second largest city of France, with a population of *ca.* 1 million.
143 The Rhône River, which flows into the Gulf of Lions, is the greatest source of freshwater and nutrients for the
144 Mediterranean Sea, with a river mean flow of $1800 \text{ m}^3 \text{ s}^{-1}$ (Pont et al., 2002). Several studies highlight the eastward
145 intrusion events from the Rhône River plume in the BoM under East and South-easterly wind conditions, which favor
146 biological productivity (Frayse et al., 2014; Gatti et al., 2006; Para et al., 2010). The biogeochemistry of the BoM is
147 complex and highly driven by hydrodynamics. For example, North-Northwesterly winds induce upwelling events
148 which bring upward cold and nutrient-rich waters (Frayse et al., 2013). Moreover, the oligotrophic Northern Current
149 occasionally intrudes into the BoM (Petrenko, 2003; Ross et al., 2016).

150 Despite the presence of several marine protected areas around the BoM (the Regional Park of Camargue, the Marine
151 protected area Côte Bleue and the National Park of Calanques), it is strongly impacted by diverse anthropogenic
152 forcing, because industrialized and urbanized areas are located all along the coast. From the land, the BoM receives
153 nutrients and organic matter from the urban area of the Aix-Marseille metropolis (Millet et al., 2018), the industrialized
154 area of Fos-sur-Mer (one of the biggest oil-based industry areas in Europe), and the Berre Lagoon, which is eutrophized
155 (Gouze et al., 2008; Fig. 2C). From the atmosphere, the BoM is subject to fine particles deposition and greenhouse gas
156 emissions (including CO_2) from the nearby urban area, and it also receives effluents from the Aix-Marseille metropolis.

157 2.3 Dataset

158 The modelled variables of the carbonate system (DIC, TA, pH and pCO_2) and chlorophyll-a are hereafter compared to
159 observations collected at the SOLEMIO station (Figs. 2C & 3), which is a component of the French national monitoring
160 network (Service d'Observation en Milieu Littoral - SOMLIT, <http://somalit.epoc.u-bordeaux1.fr/fr/>). Major
161 biogeochemical parameters have been recorded since 1994. Carbonate chemistry variables (pH , pCO_2 , DIC and TA)
162 have been available since 2016, every two weeks.

163 2.4 Design of numerical experiments

164 In the present work, the Eco3M-CarbOx model was run for the whole year of 2017. This year was chosen because *in*
165 *situ* data of carbonate systems (DIC, TA, pH and pCO_2) are available for the whole year at the SOLEMIO station (Fig.
166 2C). The biogeochemical variables were initialized using *in situ* data from winter conditions (Tab. B1, Appendix B).
167 The model was forced by time-series of sea surface temperature and salinity, wind (at 10 m), light, and atmospheric
168 CO_2 concentrations. The sea temperature time-series is from *in situ* hourly data recorded at the Planier station (Fig.
169 2C). For salinity, hourly *in situ* data from the SOLEMIO station and from the CARRY buoy were used (Fig. 2C). Wind
170 and light hourly time-series were extracted from the WRF meteorological model at the SOLEMIO station (Yohia,
171 2017). Finally, we used hourly atmospheric CO_2 values from *in situ* measurements recorded at the *Cinq Avenues* station
172 (CAV station, Fig. 2B) by the AtmoSud Regional Atmospheric Survey Network, France (<https://www.atmosud.org>).
173 This simulation is the reference simulation (noted S0). As highlighted previously, Rhône River plume intrusions (due
174 to wind-specific conditions) have an impact on the dynamics of primary production (Frayssé et al., 2014; Ross et al.,
175 2016) and then on the seawater carbonate system. Moreover, the seawater temperature and atmospheric CO_2 variations
176 control the seawater CO_2 dynamics *via* the solubility equilibrium and gas exchange with the atmosphere (Middelburg,
177 2019). In order to quantify the impact of different forcing, several simulations (hereafter noted S), which are
178 summarized in Table 1, were conducted:

- 179 • Impact of seawater temperature increase, S1: the forcing time-series of *in situ* temperatures was shifted by $+1.5^\circ C$
180 (Cocco et al., 2013).
- 181 • Impact of wind events: a first simulation S2 was run with a constant wind intensity of 7 m s^{-1} (2017 annual average
182 wind speed) throughout the year and a second one (S3) with two three-day periods of strong wind speed (20 m s^{-1})
183 representative of short bursts of Mistral (data not shown) starting on May 15th and August 15th, and a constant value
184 of 7 m s^{-1} the rest of the year.
- 185 • Impact of nutrient supply (nitrate) during a Rhône River plume intrusion (S4). A threshold of 37 has been chosen
186 to identify the presence of low-salinity waters from the Rhône River plume in the forcing file of salinity. Here, the
187 contents of nitrate supplied by the river depends on the salinity. A relationship between these two variables was
188 then established for the SOLEMIO point from the MARS3D-RHOMA coupled physical and biogeochemical model
189 (Frayssé et al., 2013; Pairaud et al., 2011). This relationship has already been used successfully to reproduce
190 realistic observed conditions in the studies of Frayssé et al. (2014) and Ross et al. (2016): $NO_{3\text{intrusion}} (\text{mmol m}^{-3}) =$
191 $-1.70 \times S + 65$.
- 192 • Non-urban atmospheric CO_2 concentrations (S5): this simulation takes into account the forcing of atmospheric CO_2
193 values measured at the *Observatoire de Haute Provence* station (OHP, Fig. 2B) located outside of the Aix-Marseille
194 metropolis from the ICOS National Network, France ([http://www.obs-hp.fr/ICOS/Plaquette-ICOS-](http://www.obs-hp.fr/ICOS/Plaquette-ICOS-201407_lite.pdf)
195 [201407_lite.pdf](http://www.obs-hp.fr/ICOS/Plaquette-ICOS-201407_lite.pdf)).

196 In this work, we calculated the daily mean values of state variables, statistical parameters and mean fluxes of modeled
197 processes throughout the year and over two main hydrological periods: the stratified and mixed water column periods.
198 The stratified water column (SWC) is defined with a temperature difference between the surface and bottom of more
199 than 0.5°C (Monterey and Levitus, 1997). For the simulated year (2017), the SWC period lasts from May 10th to
200 October 20th. The mixed water column (MWC) period corresponds to the rest of the year.

201 3. Results

202 3.1 Model skills

203 Following the recommendations of Rykiel (1996), three criteria were considered to evaluate the performance of our
204 model:

- 205 - Does the model reproduce the timing of the observed variations of carbonate system at the seasonal time
206 scale?
- 207 - Does the model reproduce the observed $p\text{CO}_2$ and $p\text{H}$ ranges at the seasonal time scale?
- 208 - Analysis of the Willmott Skill Score (WSS): this index is an objective measurement of the degree of
209 agreement between the modeled results and the observed data. A correct representation of observations by
210 the model is achieved when this index is higher than 0.70 (Willmott, 1982).

211 Over most of the studied period, the model simulates lower chlorophyll-a concentrations than the *in situ* observations,
212 especially during the MWC period (Fig. 3A). Two maxima of chlorophyll-a concentrations are observed *in situ*: the
213 first one at *ca.* 1.71 mg m⁻³ in March and the second one at *ca.* 0.68 mg m⁻³ in May. They are both linked to Rhône
214 River plume intrusions. Several *in situ* maxima between 0.50 and 0.70 mg m⁻³ are observed between March and April
215 (at the end of the MWC period), and they signaled the spring bloom event (Tab. 2 & Fig. 3A). The biogeochemical
216 model quantitatively reproduces the spring bloom observed at the end of the MWC period (Fig. 3A) with a maximum
217 value of *ca.* 0.69 mg m⁻³. The model does not catch the two aforementioned maxima of chlorophyll, and it contains a
218 low WSS and a strong bias (0.37 and +0.22 mg m⁻³, respectively - Tab. 2).

219 On the whole, the seasonal variations of the seawater $p\text{CO}_2$ are correctly simulated by the biogeochemical model (Fig.
220 3B), even if the values are rather overestimated during the MWC period. From January to February, the model
221 reproduces the slight decrease in the observed $p\text{CO}_2$ and from February to March the increase in $p\text{CO}_2$ even if the latter
222 modelled remains smaller. In mid-April, during the simulated spring bloom period, the observed drop in $p\text{CO}_2$ and
223 increase in $p\text{H}$ are also spotted in the model (Fig. 3B & 3C). The model especially succeeds in reproducing the observed
224 increase in relation to high temperatures during the SWC period. The reduction of the CO_2 solubility due to thermal
225 effects mostly explains the increase in $p\text{CO}_2$ during the SWC period. The strong standard deviation of modeled values
226 during the SWC period can be explained by the rapid changes in temperature probably due to upwelling usually
227 occurring at this time of the year (Millot, 1990). The range of modeled $p\text{CO}_2$ values (345 - 503 μatm) encompasses
228 the range of observed values (358 - 471 μatm ; Tab. 2). The statistical analysis provides a mean bias of +23 μatm , and
229 a WSS of 0.69 (Tab. 2).

230 The seasonal dynamic of $p\text{H}$ is mostly reproduced by the model, and in particular, the decrease during the SWC period
231 (Fig. 3C). However, the modelled $p\text{H}$ is generally underestimated throughout the year, except during the SWC period,
232 with a mean bias of -0.015 (Tab. 2). The seasonal range is captured by the model with a minimum value during the
233 SWC period (7.994 *vs.* 8.014 for observations; Tab.2) and a maximum one during the MWC period (8.137 *vs.* 8.114
234 for observations; Tab.2). The statistical analysis highlights an index of agreement between the *in situ* data and the
235 model outputs higher than 0.70 (Tab. 2).

236 The seasonal variations of DIC show the highest values during the MWC period and a decrease (resp. increase) during
237 the beginning (resp. the end) of the SWC period (Fig. 3D). The lowest values are observed during September. The
238 Eco3M-CarbOx model closely matches the seasonal dynamic by reproducing the range of extreme observed values
239 (Tab. 2). The mean bias is also small ($-8.48 \mu\text{mol kg}^{-1}$, Tab. 2). More than 70% (0.73, Tab. 2) of modeled DIC
240 concentrations are in statistical agreement with the corresponding observations.

241 The seasonal cycle of measured TA does not show a clear pattern (Fig. 3E). Large variations of values ranging between
242 2561 and 2624 $\mu\text{mol kg}^{-1}$ (Tab. 2) are observed, whatever the hydrological season is that is considered. The
243 biogeochemical model provides almost constant values around 2570 $\mu\text{mol kg}^{-1}$ all along the year, which is lower than
244 *in situ* data. With a low WSS index of agreement and a large mean bias (Tab. 2), the model is not able to confidently
245 reproduce the observed variations of TA (Fig. 3E & Tab. 2).

246 3.2 Carbon fluxes and budgets

247 For the year 2017, the values of temperature vary between 13.3°C and 25.9°C (Fig. 4A). The DIC variations closely
248 match those of temperature (correlation coef. -0.75). For example, the spring increase in temperature leads to a decrease
249 in DIC concentrations (Figs. 4A & 4C), and the minimum values are reached at the end of SWC period. Over the
250 simulated period, the air-sea CO₂ fluxes (F_{aera}) vary between -14 and 17 $\text{mmol m}^{-3} \text{d}^{-1}$, with a weakly positive annual
251 budget of +6 $\text{mmol m}^{-3} \text{y}^{-1}$ (or +0.017 $\text{mmol m}^{-3} \text{d}^{-1}$, Tab. 3). Then, the BoM waters would act as a net source of CO₂
252 to the atmosphere on an annual basis. However, on a seasonal basis, the BoM waters would change from a net sink
253 during the MWC period ($F_{\text{aera}} < 0$; Tab. 3) to a net source during the SWC one ($F_{\text{aera}} > 0$; Tab. 3).

254 On an annual basis, the gross primary production (GPP) and total respiration (R) are balanced, leading to a null average
255 net ecosystem production (NEP, $\text{NEP} = \text{GPP} - \text{R}$) (Fig. 4F & Tab. 3). The intensity of autotroph respiration (R_a) is lower
256 than that of primary production (annual mean of 0.065 vs. -0.413 $\text{mmol m}^{-3} \text{d}^{-1}$, respectively - Tab. 3). While the
257 zooplankton and bacterial respiration account for an average of 0.348 $\text{mmol m}^{-3} \text{d}^{-1}$ (Tab. 3). On a seasonal basis, the
258 model highlights an ecosystem dominated by autotrophy during the MWC period ($\text{NEP} > 0$; Tab. 3) and heterotrophy
259 during the SWC period with higher fluxes values ($\text{NEP} < 0$; Tab. 3). The biogeochemical fluxes show the strongest
260 variations along the SWC period, following those of temperature (Fig. 4F). The maximum GPP occurs in April and is
261 correlated with the maximum chlorophyll concentration. At this time, the ecosystem is autotroph ($\text{NEP} > 0$; Figs. 4B &
262 4F), and is a net sink for atmospheric CO₂, which explains the DIC and seawater $p\text{CO}_2$ decreases during the bloom
263 period (Figs. 4C, 4D & 4E)

264 When looking in details at the temperature and salinity 2017 time-series (Fig. 4A), several crucial events can be seen
265 occurring, including freshwater intrusions (e.g. March 15th and May 6th) into the BoM and large variations of
266 temperature in relation with upwelling events or latent heat losses due to wind bursts. The largest freshwater intrusion
267 from the Rhône River plume occurs in mid-March, with a minimum observed salinity of *ca.* 32.5 at the SOLEMIO
268 station (Fig. 4A). During this event, the seawater $p\text{CO}_2$ decreases and $p\text{H}$ increases concomitantly (Figs. 4C & 4D).
269 Then, seawater appears to be temporarily under-saturated in CO₂ and the BoM waters thus acts as a sink for atmospheric
270 CO₂ at the time of intrusion (Fig. 4E).

271 During the SWC period, upwelling events quickly cool the surface seawater. In two days, from July 25th to 27th, the
272 water temperature drops from 24.7°C to 16.9°C (Fig. 4G). The decrease in temperature corresponds to the increase in
273 DIC concentrations (Fig. 4I). Concomitantly, the values of seawater $p\text{CO}_2$ decrease from 497 to 352 μatm and $p\text{H}$
274 increase from 7.99 to 8.12 (Figs. 4I & 4J). This event quickly changes the BoM waters from a source to a sink for
275 atmospheric CO₂ (from +17 to -14 $\text{mmol m}^{-3} \text{d}^{-1}$, Fig. 4K), and also from a net heterotroph to a net autotroph ecosystem
276 (Fig. 4L).

277 3.3 Impact of external forcing on the dynamics of carbonate system

278 3.3.1 Temperature increase

279 Here we compare the reference simulation S0 with the S1 simulation (seawater temperature elevation of 1.5°C - Fig.
280 5). During the year, there are few changes on the carbonate system variables such as the $p\text{CO}_2$ and $p\text{H}$ (data not shown).
281 The main alterations occur during the blooms of phytoplankton. The simulated bloom of phytoplankton occurs later,
282 at beginning of May, for both diatoms and picophytoplankton, with a maximum value of chlorophyll at 1.4 and 0.4 mg
283 m^{-3} , respectively (Figs. 5A & 5F).

284 As both the limitations due to light and nutrients remain about the same during the simulations S0 and S1, this
285 counterintuitive occurrence of bloom relative to changes in temperature is mainly explained by the temperature limiting
286 function, which depends on the optimal temperature of growth (T_{opt}). For the picophytoplankton, from January to April,
287 the increase of 1.5°C drastically reduces the limitation by temperature (Fig. 5C), because the temperature is closer to
288 the optimal temperature ($T_{\text{opt}}=16^\circ\text{C}$, Tab. A4) during S1 than S0. In the S0 simulation, the temperature reaches T_{opt} *ca.*
289 April 15th and it induces the bloom, while at the same time in S1 the temperature moves slightly away from T_{opt} and it
290 does not enable the triggering of a bloom. At the time of the bloom in S1, the opposite configuration occurs. In S0, the
291 ambient temperature is again far from T_{opt} , explaining the absence of bloom, while in the S1 the ambient temperature
292 is closer to T_{opt} enabling the occurrence of bloom. The picophytoplankton bloom then occurs later in the warm
293 simulation S1 than in the reference simulation S0 (Fig. 5A). The duration and termination of bloom is controlled both
294 by the nutrients availability and the temperature (Figs. 5C & 5D). Inversely, from January to April, the diatoms' growth
295 limitation by temperature is strengthened in the warm simulation S1 (Fig. 5H), because the resulting ambient
296 temperature is further from the optimum temperature ($T_{\text{opt}}=13^\circ\text{C}$, Tab. A4) than that in the reference simulation S0.
297 This induces a slower growth of diatoms and a delay of the maximum concentration (Fig. 5F). Afterwards the
298 photosynthesis is mainly limited by temperature (Fig. 5H).

299 The ecosystem is net autotroph at the time of blooms whatever the simulation considered ($\text{NEP}>0$; Fig. 5E) and the
300 quantity of DIC (not shown) fixed through autotroph processes is larger than that released by heterotroph processes.
301 During the short period of bloom, the seawater $p\text{CO}_2$ decreases, leading to some negative air-sea fluxes (*i.e.* an oceanic
302 sink for atmospheric CO_2). In the warm simulation, the later occurrence of bloom enables the period of the spring sink
303 to extend by *ca.* three weeks over May relative to the reference simulation (Fig. 5J).

304 3.3.2 Wind speed

305 The Bay of Marseille is periodically under the influence of strong wind events (Millot, 1990). Here we compare two
306 simulations: one with a constant wind value (S2) and the other one with two wind events that occur in May and August
307 (S3) (Figs. 6A & D). The result of this numerical experiment shows that the stronger the wind speed is, the higher the
308 air-sea fluxes are, mainly owing to the increase in gas transfer velocity. Depending on the gradient of CO_2 between
309 seawater and the atmosphere, strong wind speeds will favor either the emission or uptake of CO_2 (Figs. 6B & E). In
310 May, with the air-sea CO_2 flux being positive, the outgassing of CO_2 to the atmosphere is enhanced leading to a
311 decrease in seawater $p\text{CO}_2$ (Fig. 6C). On the contrary, in August the oceanic sink of atmospheric CO_2 is amplified
312 which leads to an increase in the seawater $p\text{CO}_2$ value (Fig. 6F).

313 3.3.3 Supply in nitrate by river inputs

314 According to the model results (Fig. 7), the occasional inputs of nitrate (S4) that are linked to Rhône River plume
315 intrusions favor primary production and they led to increased chlorophyll concentrations (Figs. 7B & 7C) five times

316 during the SWC period. These blooms, as seen previously, lead to a decrease (resp. increase) in the seawater $p\text{CO}_2$
317 (resp. $p\text{H}$) (Figs. 7E & 7F). It can be noted that with the strongest river supply at mid-March (Figs. 7A & 7B) the
318 occurrence of the spring bloom is earlier (Fig. 7C) than that occurring in the reference simulation (S0). The time lag
319 between river nutrient supply and bloom is due to the temperature limitation (Fig. 4C). During blooms occurring within
320 the SWC period following intrusions, the DIC concentrations are generally lower than those of the reference
321 simulation, as in the case of the bloom of mid-May (decrease by *ca.* $15 \mu\text{mol kg}^{-1}$, Fig. 7J), due to the autotroph
322 processes dominating the heterotroph ones. In turn, the seawater $p\text{CO}_2$ drops by *ca.* $30 \mu\text{atm}$ (Fig. 7K) and $p\text{H}$ increases
323 by *ca.* 0.030 (Fig. 7L). Nitrate inputs, favoring primary production, reduce the source of CO_2 to the atmosphere and
324 intensify the sink of atmospheric CO_2 into the waters of BoM (Figs. 7E & 7K).

325 **3.3.4 Urban air CO_2 concentrations**

326 The Aix-Marseille metropolis is strongly subject to urban emissions to the atmosphere (Xueref-Remy et al., 2018a).
327 The seasonal variability of atmospheric CO_2 concentrations at the urban site (CAV station, Fig. 2) is much higher than
328 that observed in a non-urban area (OHP station, Fig. 2), especially during the MWC period (Fig. 8A): CO_2
329 concentrations vary between 379 and $547 \mu\text{atm}$ at the CAV station and between 381 and $429 \mu\text{atm}$ at the OHP station.
330 Moreover, in winter the atmospheric $p\text{CO}_2$ is higher in the urban area than non-urban area, whereas in summer those
331 of both areas are quite close. These differences in the seasonal pattern and between areas are usually explained by (i)
332 the thinner atmospheric boundary layer, (ii) the decreased fixation of CO_2 by terrestrial vegetation, and (iii) the greater
333 influence of anthropogenic activities by emissions from heating (Xueref-Remy et al., 2018b). Forcing the model by
334 atmospheric $p\text{CO}_2$ values from urban or non-urban site can lead to significant differences in the values of the seawater
335 $p\text{CO}_2$ during the MWC period especially. The air-sea gradient of $p\text{CO}_2$ is higher when using a forcing derived from
336 the CO_2 concentrations originating from an urban area than from non-urban area, which strengthens the sink of
337 atmospheric CO_2 into the waters of BoM. The seawater $p\text{CO}_2$ is then lower with non-urban area pressure (S5) than
338 with urban area pressure (S0), because of lower CO_2 solubility in the BoM (Fig. 8B).

339 **4. Discussion**

340 **4.1 Model performance**

341 The evaluation of model skill *vs. in situ* data highlights that the modeled $p\text{H}$, $p\text{CO}_2$, DIC are in acceptable agreement
342 with observations (Fig. 3). The seasonal variations observed for the different variables are captured by the model,
343 including for example the seasonal decrease in DIC and $p\text{H}$ during the SWC period, in relation to the increase in $p\text{CO}_2$,
344 and the inverse scenario during the MWC period. The chlorophyll content variability is not well reproduced, especially
345 during spring (Fig. 3A), even taking into account the nitrate supply from the Rhône River plume intrusion (Fig. 7C).
346 This is due to the multiple origins of chlorophyll, organic matter, and nutrients in the BoM that are not accounted for
347 in the Eco3M-CarbOx model: autochthonous marine production, and allochthonous origins from the Rhône and
348 Huveaune River plumes (Frayssé et al., 2013). The observed variations and levels of TA are not correctly simulated
349 by the model (Fig. 3F). The study of Soetaert et al. (2007) highlights that the main variations of TA in the marine
350 coastal zones are linked to freshwater supplies and marine sediments. The present study does not take into account the
351 inputs of TA from the Rhône River and the water-sediment interface, and it may explain why the TA variable is not
352 correctly predicted by our model.

353 4.2 Contribution of physical and biogeochemical processes to the variability of carbonate system

354 The contribution of each biogeochemical process to the DIC variability can be assessed using the presented model: the
355 aeration process contributes to 78% of the DIC variations and biogeochemical processes together to 22% (Tab. 3). As
356 mentioned by Wimart-Rousseau et al. (2020), the model suggests that the seawater $p\text{CO}_2$ variations and associated
357 fluxes would be mostly driven by the seawater temperature dynamics. Moreover, the seasonal variations of the air-sea
358 CO_2 flux are in agreement with some previous field studies (De Carlo et al., 2013; Wimart-Rousseau et al., 2020),
359 which measured a weak oceanic sink for atmospheric CO_2 during winter and a weak source to the atmosphere during
360 summer.

361 The model results reveal that temperature would play a crucial role in controlling two counterbalanced processes: (1)
362 the carbonate system equilibrium and (2) the phytoplankton growth. The increase in temperature during SWC leads to
363 a higher $p\text{CO}_2$ in seawater due to the decrease in the CO_2 solubility (Middelburg, 2019) and, at the same time, the
364 fixation of DIC by phytoplankton is favored, leading to a decrease in the $p\text{CO}_2$ level. The imbalance between the latter
365 two processes leads to a change in the ecosystem status (autotrophic or heterotrophic) and the corresponding behavior
366 as a sink or source to the atmosphere. In case of a 1.5°C rise over the whole year, the temperature variation has a very
367 small impact on the carbonate system dynamics. However, it favors the autotrophic processes and strengthens the
368 oceanic sink of atmospheric CO_2 during the bloom of phytoplankton (Figs. 5E & 5J).

369 4.3 Contribution of the external forcing to the variability of carbonate system

370 In line with several previous works on the Northwestern Mediterranean Sea (De Carlo et al., 2013; Copin-Montégut et
371 al., 2004; Wimart-Rousseau et al., 2020), the model also suggests that the status of the Bay of Marseille regarding sink
372 or source for CO_2 could change at high temporal frequency (*i.e.* hours to days). Bursts of North, Northwestern winds,
373 lead to sudden and sharp decreases in seawater temperature (<2 days, Fig. 4G) either directly by latent heat loss through
374 evaporation at the surface (Herrmann et al., 2011) or indirectly by creating upwelling (Millot, 1990), with the
375 consequences of decrease in the seawater $p\text{CO}_2$ values (Fig. 4J) and *in fine*, an alteration of the CO_2 air-sea fluxes.
376 Model results suggest that the fast variations of temperature could lead to rapid changes of the sink vs. source status in
377 this coastal zone (Fig. 4K). Moreover, Frayse et al. (2013) highlight that upwelling in the BoM favors ephemeral
378 blooms of phytoplankton by nutrient supplies up to euphotic layer and would, in turn, contribute to the seawater $p\text{CO}_2$
379 decrease. North, and Northwestern winds through latent heat losses and/or upwelling events could then enhance the
380 sink for atmospheric CO_2 due to the temperature drop and nutrients inputs. However, these results remain to be
381 preliminary because in our experimental design only the cooling effect of upwelling on the carbonate balance is taken
382 into account. But concomitantly, upwelling usually bring nutrients and DIC at the surface and these supplies could
383 also perturb the balance of the carbonate system. A next coupling of the Eco3M-CarbOx model with a tridimensional
384 hydrodynamic model would enable to certainly embrace the multiple effects of upwelling on the dynamics of the
385 carbonate system in this area and refine the results presented in this study.

386 High wind speeds ($>7 \text{ m s}^{-1}$) amplified considerably the gaseous exchange of CO_2 (De Carlo et al., 2013; Copin-
387 Montégut et al., 2004; Wimart-Rousseau et al., 2020). The model highlights that a strong wind event of 3 days has a
388 significant impact on the seawater $p\text{CO}_2$ values during a longer period of *ca.* 15 days (Fig. 6). A combination of high
389 atmospheric $p\text{CO}_2$ value and high wind speed would then favor the sink for CO_2 into the waters of the BoM. The
390 aeration process depends also on the choice of the formulation of the gas transfer velocity (k_{600}). In this study, the
391 formulation of Wanninkhof (1992) is used and depends of the wind speed at 10 m above the water surface. However,
392 the current velocity could favor the gas exchange and suspended matter concentration could limit the gas exchange
393 (Abril et al., 2009; Upstill-Goddard, 2006; Zappa et al., 2003). Due to the important heterogeneity of physical and

394 biogeochemical forcings in coastal zones, other factors that control the air-sea gas exchange should certainly be taken
395 into account.

396 The simulation with intrusions of the Rhône River plume shows that inputs of nitrate cause a drop of seawater $p\text{CO}_2$
397 owing to nutrients supply favoring the phytoplankton development (Fig. 7). In this scenario, the oceanic sink of
398 atmospheric CO_2 is enhanced. But rivers also supply TA (*e.g.* Gemayel et al., 2015; Schneider et al., 2007) and DIC
399 (*e.g.* Sempéré et al., 2000) that shift the carbonate system equilibrium toward a $p\text{CO}_2$ decrease and a DIC increase
400 (Middelburg, 2019). Taking into account these further supplies may sensibly modify the modeled carbonate balance
401 in the BoM. A next step to the present work will be to design more realistic numerical experiments to refine the results
402 obtained in this preliminary study. The intrusions of Rhône River plume also induce a salinity decrease of the BoM
403 waters, which leads to drop the $p\text{CO}_2$ levels in the model. This drop of $p\text{CO}_2$ is due to the decrease in the CO_2 solubility
404 when salinity decreases (Middelburg, 2019).

405 In the scenario of forcing the model by using urban atmospheric $p\text{CO}_2$ time-series, the air-sea gradient increases and
406 then, it enhances the status of the BoM as a sink for atmospheric CO_2 . As suggested by the *in situ* study of Wimart-
407 Rousseau et al. (2020), the Eco3M-Carbox model highlights the crucial role of the coastal ocean in urbanized area,
408 with an increase in atmospheric CO_2 , the CO_2 uptake by the costal ocean may increase. This results is in line with
409 studies of Andersson and Mackenzie (2004) and Cai (2011) that predict an increase in the intensity of CO_2 sink and a
410 potential threat to coastal marine biodiversity in coastal areas owing to high atmospheric CO_2 levels.

411 5. Conclusion

412 A marine carbonate chemistry module was implemented in the Eco3M-CarbOx biogeochemical model and evaluated
413 against *in situ* data available in the Bay of Marseille (Northwestern Med. Sea) over the year 2017. The model correctly
414 simulates the values ranges and seasonal dynamics of most of variables of the carbonate system except for the total
415 alkalinity. Several numerical experiments were also conducted to test the sensitivity of carbon balance to physical
416 processes (temperature and salinity), biogeochemical processes (GPP and respiration processes) and external forcing
417 (wind, river intrusion and atmospheric CO_2). This set of numerical experiments shows that the Eco3M-CarbOx model
418 provides expected responses in the alteration of the marine carbonate balance regarding each of the considered
419 perturbation.

420 On the whole, the model results suggest that the carbonate system is mainly driven by the seawater temperature
421 dynamics. At a seasonal scale, the BoM marine waters appear to be a net sink of atmospheric CO_2 and a dominant
422 autotroph ecosystem during the MWC period, and a net source of CO_2 to the atmosphere during the SWC period,
423 which is mainly characterized by a dominance of heterotroph processes. However, the model results highlight that
424 sharp seawater cooling observed within the SWC period and probably owing to upwelling events, cause the CO_2 status
425 of the BoM marine waters to change from a source to the atmosphere to a sink into the ocean within a few days.
426 External forcing as the temperature increases leads to a delay in the bloom of phytoplankton. Strong wind events
427 enhance the gas exchange of CO_2 with the atmosphere. A Rhône River plume intrusion with input of nitrate favors
428 $p\text{CO}_2$ decreases, and the sink of atmospheric CO_2 into the BoM waters is enhanced. The higher atmospheric $p\text{CO}_2$
429 values from the urban area intensify the oceanic sink of atmospheric CO_2 .

430 The BoM biogeochemical functioning is mainly forced by wind-driven hydrodynamics (upwelling, downwelling),
431 urban rivers, wastewater treatment plants, and atmospheric deposition (Fraysse et al., 2013). In addition, Northern
432 Current and Rhône River plume intrusions frequently occurred (Fraysse et al., 2014; Ross et al., 2016). Moreover, the
433 BoM harbors the second bigger metropolis of France (Marseille) that is impacted by many harbor activities. The next

434 step of this study will be to couple the Eco3M-CarbOx biogeochemical model to a 3D hydrodynamic model that will
435 mirror the complexity of the BoM functioning. In this way, the contributions of hydrodynamic, atmospheric, anthropic,
436 and biogeochemical processes to the DIC variability will be able to be determined with higher refinement and realism,
437 and an overview of the air-sea CO₂ exchange could be made at the scale of the Bay of Marseille. The main results of
438 our study could be transposed to other coastal sites that are also impacted by urban and anthropic pressures. Moreover,
439 in this paper we highlighted that fast and strong variations of *p*CO₂ values occur, so thus it is essential to acquire more
440 *in situ* values at high frequency (at least with an hourly resolution) to understand the rapid variations of the marine
441 carbon system at these short spatial and temporal scales.

442

443 **Acknowledgements**

444 We thank the National Service d'Observation en MILieu Littoral (SOMLIT) for its permission to use SOLEMIO data.
445 We wish to thank the crewmembers of the R.V. 'Antedon II', operated by the DT-INSU, for making these samplings
446 possible. We wish to acknowledge the team of the SAM platform (Service Atmosphère Mer) of MIO institute for their
447 helping in field work. For the collection and analyses of the seawater sample, we thank Michel Lafont and Véronique
448 Lagadec of the PACEM (Plateforme Analytique de Chimie des Environnements Marins) platform of MIO institute
449 and also the SNAPO-CO2 at LOCEAN, Paris. The SNAPO-CO2 service at LOCEAN is supported by CNRS-INSU
450 and OSU Ecce-Terra.
451 We acknowledge the staff of the "Cluster de calcul intensif HPC" Platform of the OSU Institut Pythéas (Aix-Marseille
452 Université, INSU-CNRS) for providing the computing facilities. We gratefully acknowledge Julien Lecubin from the
453 Service Informatique de OSU Institut Pythéas (SIP) for their technical assistance. Moreover, we thank Camille
454 Mazoyer and Claire Seceh for their contribution on the Eco3M-CarbOx model development.

455 **Financial support**

456 This study is part of the AMC project (Aix-Marseille Carbon Pilot Study, 2016-2019) funded and performed in the
457 framework of the Labex OT-MED (ANR-11-LABEX-0061, part of the "Investissement d'Avenir" program through
458 the A*MIDEX project ANR-11-IDEX-0001-02), funded by the French National Research Agency (ANR). The project
459 leading to this publication has received funding from the European FEDER Fund under project 1166-39417.

460 **Code availability**

461 Eco3M is freely available under CeCILL license agreement (a French equivalent to the L-GPL license;
462 http://cecill.info/licences/Licence_CeCILL_V1.1-US.html; last access: 10 February 2020). The Eco3M-CarbOx
463 model is written in Fortran-90/95 and the plotting code is written in Matlab[®]. The exact version of the model used to
464 produce the results presented in this paper is archived on Zenodo (DOI: 10.5281/zenodo.3757677) (last access: 24
465 August 2020). A short User Manual is given in the Appendix C of this study.

466

- 468 Abril, G., Commarieu, M. V., Sottolichio, A., Bretel, P. and Guérin, F.: Turbidity limits gas exchange in a large
469 macrotidal estuary, *Estuar. Coast. Shelf Sci.*, 83, 342–348, doi:10.1016/j.ecss.2009.03.006, 2009.
- 470 Allen, M. R., Frame, D. J., Huntingford, C., Jones, C., Lowe, J. A., Meinshausen, M. and Meinshausen, N.: Warming
471 caused by cumulative carbon emissions towards the trillionth tonne, *Nature*, 458, 1163–1166,
472 doi:10.1038/nature08019, 2009.
- 473 Andersson, A. J. and Mackenzie, F. T.: Shallow-water oceans: a source or sink of atmospheric CO₂?, *Front. Ecol.*
474 *Environ.*, 2(7), 348–353, doi:10.1890/1540-9295, 2004.
- 475 Andersson, A. J. and Mackenzie, F. T.: Revisiting four scientific debates in ocean acidification research,
476 *Biogeosciences*, 9(3), 893–905, doi:10.5194/bg-9-893-2012, 2012.
- 477 Auger, P. A., Diaz, F., Ulses, C., Estournel, C., Neveux, J., Joux, F., Pujo-Pay, M. and Naudin, J. J.: Functioning of
478 the planktonic ecosystem on the Gulf of Lions shelf (NW Mediterranean) during spring and its impact on the carbon
479 deposition: a field data and 3-D modelling combined approach, *Biogeosciences*, 8(11), 3231–3261, doi:10.5194/bg-8-
480 3231-2011, 2011.
- 481 Baklouti, M., Faure, V., Pawlowski, L. and Sciandra, A.: Investigation and sensitivity analysis of a mechanistic
482 phytoplankton model implemented in a new modular numerical tool (Eco3M) dedicated to biogeochemical modelling.
483 *Prog. Oceanogr.*, 71(1), 34–58, doi:10.1016/j.pocean.2006.05.003, 2006.
- 484 Borges, A. V and Abril, G.: Carbon dioxide and methane dynamics in estuaries, in *Treatise on Estuarine and Coastal*
485 *Science*, edited by E. Wolanski and D. McLusky, pp. 119–161, Academic Press, Waltham., 2011.
- 486 Le Borgne, R.: Zooplankton production in the eastern tropical Atlantic Ocean: Net growth efficiency and P:B in terms
487 of carbon, nitrogen, and phosphorus, *Limnol. Oceanogr.*, 27(4), 681–698, doi:10.4319/lo.1982.27.4.0681, 1982.
- 488 Le Borgne, R. and Rodier, M.: Net zooplankton and the biological pump: a comparison between the oligotrophic and
489 mesotrophic equatorial Pacific, *Deep Sea Res. Part II*, 44(9), 2003–2023, doi:10.1016/S0967-0645(97)00034-9, 1997.
- 490 Cai, W.-J.: Estuarine and coastal ocean carbon paradox: CO₂ sinks or sites of terrestrial carbon incineration?, *Ann.*
491 *Rev. Mar. Sci.*, 3(1), 123–145, doi:10.1146/annurev-marine-120709-142723, 2011.
- 492 Cai, W.-J., Hu, X., Huang, W.-J., Murrell, M. C., Lehrter, J. C., Lohrenz, S. E., Chou, W.-C., Zhai, W., Hollibaugh, J.
493 T., Wang, Y., Zhao, P., Guo, X., Gundersen, K., Dai, M. and Gong, G.-C.: Acidification of subsurface coastal waters
494 enhanced by eutrophication, *Nat. Geosci.*, 4(11), 766–770, doi:10.1038/ngeo1297, 2011.
- 495 Campbell, R., Diaz, F., Hu, Z., Doglioli, A., Petrenko, A. and Dekeyser, I.: Nutrients and plankton spatial distributions
496 induced by a coastal eddy in the Gulf of Lion. Insights from a numerical model, *Prog. Oceanogr.*, 109, 47–69,
497 doi:10.1016/j.pocean.2012.09.005, 2013.
- 498 De Carlo, E. H., Mousseau, L., Passafiume, O., Drupp, P. S. and Gattuso, J.-P.: Carbonate Chemistry and Air–Sea CO₂
499 Flux in a NW Mediterranean Bay Over a Four-Year Period: 2007–2011, *Aquat. Geochemistry*, 19(5–6), 399–442,
500 doi:10.1007/s10498-013-9217-4, 2013.
- 501 Chen, C.-T. A. and Borges, A. V: Deep-Sea Research II Reconciling opposing views on carbon cycling in the coastal
502 ocean : Continental shelves as sinks and near-shore ecosystems as sources of atmospheric CO₂, *Deep Sea Res. II*, 56,
503 578–590, doi:10.1016/j.dsr2.2009.01.001, 2009.
- 504 Chen, C.-T. A., Huang, T.-H., Chen, Y.-C., Bai, Y., He, X. and Kang, Y.: Air–sea exchanges of CO₂ in the world’s
505 coastal seas, *Biogeosciences*, 10(10), 6509–6544, doi:10.5194/bg-10-6509-2013, 2013.
- 506 Cloern, J. E.: Our evolving conceptual model of the coastal eutrophication problem, *Mar. Ecol. Prog. Ser.*, 210, 223–
507 253, doi:10.3354/meps210223, 2001.
- 508 Cloern, J. E., Foster, S. Q. and Kleckner, A. E.: Phytoplankton primary production in the world’s estuarine-coastal
509 ecosystems, *Biogeosciences*, 11, 2477–2501, doi:10.5194/bg-11-2477-2014, 2014.
- 510 Cocco, V., Joos, F., Steinacher, M., Frölicher, T. L., Bopp, L., Dunne, J., Gehlen, M., Heinze, C., Orr, J., Oschlies, A.,
511 Schneider, B., Segschneider, J. and Tjiputra, J.: Oxygen and indicators of stress for marine life in multi-model global
512 warming projections, *Biogeosciences*, 10(3), 1849–1868, doi:10.5194/bg-10-1849-2013, 2013.
- 513 Copin-Montégut, C., Bégovic, M. and Merlivat, L.: Variability of the partial pressure of CO₂ on diel to annual time
514 scales in the Northwestern Mediterranean Sea, *Mar. Chem.*, 85(3), 169–189, doi:10.1016/j.marchem.2003.10.005,
515 2004.
- 516 Dickson, A. G.: Standard potential of the reaction: $\text{AgCl}_{(s)} + 12\text{H}_2\text{(g)} = \text{Ag}_{(s)} + \text{HCl}_{(aq)}$, and the standard acidity
517 constant of the ion HSO_4^- in synthetic sea water from 273.15 to 318.15 K, *J. Chem. Thermodyn.*, 22(2), 113–127,
518 doi:10.1016/0021-9614(90)90074-Z, 1990a.
- 519 Dickson, A. G.: Thermodynamics of the dissociation of boric acid in synthetic seawater from 273.15 to 318.15 K,
520 *Deep Sea Res.*, 37(5), 755–766, doi:10.1016/0198-0149(90)90004-F, 1990b.
- 521 Dickson, A. G. and Riley, J. P.: The estimation of acid dissociation constants in sea-water media from potentiometric
522 titrations with strong base. II. The dissociation of phosphoric acid, *Mar. Chem.*, 7(2), 101–109, doi:10.1016/0304-
523 4203(79)90002-1, 1979.
- 524 Doney, S. C., Tilbrook, B., Roy, S., Metzl, N., Le Quéré, C., Hood, M., Feely, R. a. and Bakker, D.: Surface-ocean
525 CO₂ variability and vulnerability, *Deep Sea Res. Part II*, 56(8–10), 504–511, doi:10.1016/j.dsr2.2008.12.016, 2009.

526 Esbaugh, A. J., Heuer, R. and Grosell, M.: Impacts of ocean acidification on respiratory gas exchange and acid-base
527 balance in a marine teleost, *Opsanus beta*, *J. Comp. Physiol. B*, 182(7), 921–934, doi:10.1007/s00360-012-0668-5,
528 2012.

529 Faure, V., Pinazo, C., Torrétou, J.-P. and Jacquet, S.: Modelling the spatial and temporal variability of the SW lagoon
530 of New Caledonia I: A new biogeochemical model based on microbial loop recycling, *Mar. Pollut. Bull.*, 61(7), 465–
531 479, doi:10.1016/j.marpolbul.2010.06.041, 2010.

532 Fraysse, M., Pinazo, C., Faure, V., Fuchs, R., Lazzari, P., Raimbault, P. and Pairaud, I.: Development of a 3D coupled
533 physical-biogeochemical model for the Marseille coastal area (NW Mediterranean Sea): What complexity is required
534 in the Coastal Zone?, *PLoS One*, 8(12), 1–18, doi:10.1371/journal.pone.0080012, 2013.

535 Fraysse, M., Pairaud, I., Ross, O. N., Faure, V. and Pinazo, C.: Intrusion of Rhône River diluted water into the Bay of
536 Marseille: Generation processes and impacts on ecosystem functioning, *J. Geophys. Res. Ocean.*, 119(10), 6535–6556,
537 doi:10.1002/2014JC010022, 2014.

538 Fukuda, R., Ogawa, H., Nagata, T. and Koike, I.: Direct Determination of Carbon and Nitrogen Contents of Natural
539 Bacterial Assemblages in Marine Environments, *Appl. Environ. Microbiol.*, 64(9), 3352–3358 [online] Available
540 from: <https://aem.asm.org/content/64/9/3352>, 1998.

541 Gatti, J., Petrenko, A., Devenon, J.-L., Leredde, Y. and Ulses, C.: The Rhône river dilution zone present in the
542 northeastern shelf of the Gulf of Lion in December 2003, *Cont. Shelf Res.*, 26(15), 1794–1805,
543 doi:10.1016/j.csr.2006.05.012, 2006.

544 Gattuso, J.-P., Frankignoulle, M. and Wollast, R.: Carbon and carbonate metabolism in coastal aquatic ecosystems,
545 *Annu. Rev. Ecol. Syst.*, 29(1), 405–34, doi:10.1146/annurev.ecolsys.29.1.405, 1998.

546 Gattuso, J.-P., Magnan, A., Bille, R., Cheung, W. W. L., Howes, E. L., Joos, F., Allemand, D., Bopp, L., Cooley, S.
547 R., Eakin, C. M., Hoegh-Guldberg, O., Kelly, R. P., Portner, H.-O., Rogers, A. D., Baxter, J. M., Laffoley, D., Osborn,
548 D., Rankovic, A., Rochette, J., Sumaila, U. R., Treyer, S. and Turley, C.: Contrasting futures for ocean and society
549 from different anthropogenic CO₂ emissions scenarios, *Science*, 349(6243), pp.aac4722, doi:10.1126/science.aac4722,
550 2015.

551 Gehlen, M., Gangstø, R., Schneider, B., Bopp, L., Aumont, O. and Ethe, C.: The fate of pelagic CaCO₃ production in
552 a high CO₂ ocean: a model study, *Biogeosciences*, 4(4), 505–519, doi:10.5194/bg-4-505-2007, 2007.

553 Gemayel, E., Hassoun, A. E. R., Benallal, M. A., Goyet, C., Rivaro, P., Abboud-Abi Saab, M., Krasakopoulou, E.,
554 Touratier, F. and Ziveri, P.: Climatological variations of total alkalinity and total dissolved inorganic carbon in the
555 Mediterranean Sea surface waters, *Earth Syst. Dyn.*, 6(2), 789–800, doi:10.5194/esd-6-789-2015, 2015.

556 Gerber, R. P. and Gerber, M. B.: Ingestion of natural particulate organic matter and subsequent assimilation, respiration
557 and growth by tropical lagoon zooplankton, *Mar. Biol.*, 52(1), 33–43, doi:10.1007/BF00386855, 1979.

558 Gouze, E., Raimbault, P., Garcia, N. and Picon, P.: Nutrient dynamics and primary production in the eutrophic Berre
559 Lagoon (Mediterranean , France), *Transitional Waters Bull.*, 2, 17–40, doi:10.1285/i18252273v2n2p17, 2008.

560 Gruber, N., Clement, D., Carter, B. R., Feely, R. A., van Heuven, S., Hoppema, M., Ishii, M., Key, R. M., Kozyr, A.,
561 Lauvset, S. K., Lo Monaco, C., Mathis, J. T., Murata, A., Olsen, A., Perez, F. F., Sabine, C. L., Tanhua, T. and
562 Wanninkhof, R. H.: The oceanic sink for anthropogenic CO₂ from 1994 to 2007, *Science*, 363(6432), 1193–1199,
563 doi:10.1126/science.aau5153, 2019.

564 Gutiérrez-Rodríguez, A., Latasa, M., Scharek, R., Massana, R., Vila, G. and Gasol, J. M.: Growth and grazing rate
565 dynamics of major phytoplankton groups in an oligotrophic coastal site, *Estuar. Coast. Shelf Sci.*, 95(1), 77–87,
566 doi:10.1016/j.ecss.2011.08.008, 2011.

567 Harrison, W. G., Harris, L. R. and Irwin, B. D.: The kinetics of nitrogen utilization in the oceanic mixed layer: Nitrate
568 and ammonium interactions at nanomolar concentrations, *Limnol. Oceanogr.*, 41(1), 16–32,
569 doi:10.4319/lo.1996.41.1.0016, 1996.

570 Herrmann, M., Somot, S., Calmanti, S., Dubois, C., and Sevault F.: Representation of spatial and temporal variability
571 of daily wind speed and of intense wind events over the Mediterranean Sea using dynamical downscaling: Impact of
572 the regional climate model configuration, *Nat. Hazards Earth Syst. Sci.*, 11, 1983–2001, doi:10.5194/nhess-11-1983-
573 2011, 2011.

574 Hoegh-Guldberg, O., Jacob, D., Taylor, M., Bindi, M., Brown, S., Camilloni, I., Diedhiou, A., Djalante, R., Ebi, K.,
575 Engelbrecht, F., Guiot, J., Hijioka, Y., Mehrotra, S., Payne, A., Seneviratne, S. I., Thomas, A., Warren, R. and Zhou,
576 G.: Impacts of 1.5°C Global Warming on Natural and Human Systems, in *Global warming of 1.5°C. An IPCC Special
577 Report on the impacts of global warming of 1.5°C above pre-industrial levels and related global greenhouse gas
578 emission pathways, in the context of strengthening the global response to the threat of climate change*, edited by V.
579 Masson-Delmotte, P. Zhai, H. O. Pörtner, D. Roberts, J. Skea, P. R. Shukla, A. Pirani, W. Moufouma-Okia, C. Péan,
580 R. Pidcock, S. Connors, J. B. R. Matthews, Y. Chen, X. Zhou, M. I. Gomis, E. Lonnoy, T. Maycock, M. Tignor, and
581 T. Waterfield, World Meteorological Organization Technical Document., 2018.

582 Kapsenberg, L., Alliouane, S., Gazeau, F., Mousseau, L. and Gattuso, J.-P.: Coastal ocean acidification and increasing
583 total alkalinity in the northwestern Mediterranean Sea, *Ocean Sci.*, 13(3), 411–426, doi:10.5194/os-13-411-2017, 2017.

584 Lacroix, G. and Grégoire, M.: Revisited ecosystem model (MODECOGeL) of the Ligurian Sea: seasonal and
585 interannual variability due to atmospheric forcing, *J. Mar. Syst.*, 37(4), 229–258, doi:10.1016/S0924-7963(02)00190-

586 2, 2002.

587 Leblanc, K., Quéguiner, B., Diaz, F., Cornet, V., Michel-Rodriguez, M., Durrieu de Madron, X., Bowler, C., Malviya,
588 S., Thyssen, M., Grégori, G., Rembauville, M., Grosso, O., Poulain, J., de Vargas, C., Pujo-Pay, M. and Conan, P.:
589 Nanoplanktonic diatoms are globally overlooked but play a role in spring blooms and carbon export, *Nat. Commun.*,
590 9(1), 953, doi:10.1038/s41467-018-03376-9, 2018.

591 Lueker, T. J., Dickson, A. G. and Keeling, C. D.: Ocean pCO₂ calculated from dissolved inorganic carbon, alkalinity,
592 and equations for K₁ and K₂: Validation based on laboratory measurements of CO₂ in gas and seawater at equilibrium,
593 *Mar. Chem.*, 70(June 2015), 105–119, doi:10.1016/S0304-4203(00)00022-0, 2000.

594 Margalef, R.: Life-forms of phytoplankton as survival alternatives in an unstable environment, edited by Gauthier-
595 Villars, *Oceanol. Acta*, 1(4), 493–509 [online] Available from: <https://archimer.ifremer.fr/doc/00123/23403/>, 1978.

596 Marty, J.-C., Chiavérini, J., Pizay, M.-D. and Avril, B.: Seasonal and interannual dynamics of nutrients and
597 phytoplankton pigments in the western Mediterranean Sea at the DYFAMED time-series station (1991–1999), *Deep
598 Sea Res. Part II Top. Stud. Oceanogr.*, 49(11), 1965–1985, doi:10.1016/S0967-0645(02)00022-X, 2002.

599 Matthews, H. D., Gillett, N. P., Stott, P. a and Zickfeld, K.: The proportionality of global warming to cumulative
600 carbon emissions., *Nature*, 459(7248), 829–32, doi:10.1038/nature08047, 2009.

601 Mella-Flores, D., Mazard, S., Humily, F., Partensky, F., Mahé, F., Bariat, L., Courties, C., Marie, D., Ras, J., Mauriac,
602 R., Jeanthon, C., Mahdi Bendif, E., Ostrowski, M., Scanlan, D. J. and Garczarek, L.: Is the distribution of
603 *Prochlorococcus* and *Synechococcus* ecotypes in the Mediterranean Sea affected by global warming?, *Biogeosciences*,
604 8(9), 2785–2804, doi:10.5194/bg-8-2785-2011, 2011.

605 Middelburg, J. J.: *Marine carbon biogeochemistry a primer for earth system scientists*, Springer B., edited by Springer
606 *Briefs in Earth System Sciences*, Springer Briefs in Earth System Sciences, 2019.

607 Millero, F. J.: *Thermodynamics Seawater - 1. The PVT Properties*, *Ocean Science and Engineering*, 7(4), 403-460
608 1982.

609 Millero, F. J.: *Thermodynamics of the carbon dioxide system in the oceans*, *Geochim. Cosmochim. Acta*, 59(4), 661–
610 677, doi:10.1016/0016-7037(94)00354-O, 1995.

611 Millet, B., Pinazo, C., Daniela, B., Remi, P., Pierre, G. and Ivane, P.: Unexpected spatial impact of treatment plant
612 discharges induced by episodic hydrodynamic events: Modelling Lagrangian transport of fine particles by Northern
613 Current intrusions in the bays of Marseille (France), edited by P. L. Science, *PLoS One*, 13(4), e0195257 (25p.),
614 doi:10.1371/journal.pone.0195257, 2018.

615 Millot, C.: The Gulf of Lions hydrodynamics, *Cont. Shelf Res.*, 10(9), 885–894, doi:10.1016/0278-4343(90)90065-T,
616 1990.

617 Monterey, G. and Levitus, S.: *Seasonal variability of mixed layer depth for the World Ocean*, NOAA Atlas NESDIS
618 14, Washington, D. C., 1997.

619 Moran, M. A.: The global ocean microbiome, *Sci. Am. Assoc. Adv. Sci.*, 350(6266), doi:10.1126/science.aac8455,
620 2015.

621 Morris, A. W. and Riley, J. P.: The bromide/chlorinity and sulphate/chlorinity ratio in sea water, *Deep Sea Res.*
622 *Oceanogr. Abstr.*, 13(4), 699–705, doi:10.1016/0011-7471(66)90601-2, 1966.

623 Mucci, A.: The solubility of calcite and aragonite in seawater at various salinities, temperatures, and one atmosphere
624 total pressure, *Am. J. Sci.*, 283(7), 780–799, doi:10.2475/ajs.283.7.780, 1983.

625 Orr, J. C., Fabry, V. J., Aumont, O., Bopp, L., Doney, S. C., Feely, R. A., Gnanadesikan, A., Gruber, N., Ishida, A.,
626 Joos, F., Key, R. M., Lindsay, K., Maier-Reimer, E., Matear, R., Monfray, P., Mouchet, A., Najjar, R. G., Plattner, G.-
627 K., Rodgers, K. B., Sabine, C. L., Sarmiento, J. L., Schlitzer, R., Slater, R. D., Totterdell, I. J., Weirig, M.-F.,
628 Yamanaka, Y. and Yool, A.: Anthropogenic ocean acidification over the twenty-first century and its impact on
629 calcifying organisms, *Nature*, 437(7059), 681–6, doi:10.1038/nature04095, 2005.

630 Pairaud, I., Gatti, J., Bensoussan, N., Verney, R. and Garreau, P.: Hydrology and circulation in a coastal area off
631 Marseille: Validation of a nested 3D model with observations, *J. Mar. Syst.*, 88(1), 20–33,
632 doi:10.1016/j.jmarsys.2011.02.010, 2011.

633 Para, J., Coble, P. G., Charrière, B., Tedetti, M., Fontana, C. and Sempéré, R.: Fluorescence and absorption properties
634 of chromophoric dissolved organic matter (CDOM) in coastal surface waters of the northwestern Mediterranean Sea,
635 influence of the Rhône River, *Biogeosciences*, 7(12), 4083–4103, doi:10.5194/bg-7-4083-2010, 2010.

636 Petrenko, A.: Variability of circulation features in the Gulf of Lion, NW Mediterranean Sea . Importance of inertial
637 currents, *Oceanol. Acta*, 26, 323–338, doi:10.1016/S0399-1784(03)00038-0, 2003.

638 Pont, D., Simonnet, J.-P. and Walter, A. V.: Medium-term changes in suspended sediment delivery to the Ocean:
639 Consequences of catchment heterogeneity and river management (Rhône River, France), *Estuar. Coast. Shelf Sci.*,
640 54(1), 1–18, doi:10.1006/ecss.2001.0829, 2002.

641 Le Quéré, C., Andrew, R. M., Friedlingstein, P., Sitch, S., Hauck, J., Pongratz, J., Pickers, P. A., Korsbakken, J. I.,
642 Peters, G. P., Canadell, J. G., Arneeth, A., Arora, V. K., Barbero, L., Bastos, A., Bopp, L., Chevallier, F., Chini, L. P.,
643 Ciais, P., Doney, S. C., Gkritzalis, T., Goll, D. S., Harris, I., Haverd, V., Hoffman, F. M., Hoppema, M., Houghton, R.
644 A., Hurtt, G., Ilyina, T., Jain, A. K., Johannessen, T., Jones, C. D., Kato, E., Keeling, R. F., Goldewijk, K. K.,

645 Landschützer, P., Lefèvre, N., Lienert, S., Liu, Z., Lombardozzi, D., Metzl, N., Munro, D. R., Nabel, J. E. M. S.,
646 Nakaoka, S.-I., Neill, C., Olsen, A., Ono, T., Patra, P., Peregon, A., Peters, W., Peylin, P., Pfeil, B., Pierrot, D., Poulter,
647 B., Rehder, G., Resplandy, L., Robertson, E., Rocher, M., Rödenbeck, C., Schuster, U., Schwinger, J., Séférian, R.,
648 Skjelvan, I., Steinhoff, T., Sutton, A., Tans, P. P., Tian, H., Tilbrook, B., Tubiello, F. N., van der Laan-Luijkx, I. T.,
649 van der Werf, G. R., Viovy, N., Walker, A. P., Wiltshire, A. J., Wright, R., Zaehle, S. and Zheng, B.: Global Carbon
650 Budget 2018, *Earth Syst. Sci. Data*, 10(4), 2141–2194, doi:10.5194/essd-10-2141-2018, 2018.

651 Raven, J. A. and Falkowski, P. G.: Oceanic sinks for atmospheric CO₂, *Plant. Cell Environ.*, 22(6), 741–755,
652 doi:10.1046/j.1365-3040.1999.00419.x, 1999.

653 Riley, J. P.: The occurrence of anomalously high fluoride concentrations in the North Atlantic, *Deep Sea Res.*
654 *Oceanogr. Abstr.*, 12(2), 219–220, doi:10.1016/0011-7471(65)90027-6, 1965.

655 Riley, J. P. and Tongudai, M.: The major cation/chlorinity ratios in sea water, *Chem. Geol.*, 2, 263–269,
656 doi:10.1016/0009-2541(67)90026-5, 1967.

657 Roobaert, A., Laruelle, G. G., Landschützer, P., Gruber, N., Chou, L. and Regnier, P.: The spatiotemporal dynamics
658 of the sources and sinks of CO₂ in the global coastal ocean, *Global Biogeochem. Cycles*, 33,
659 doi:10.1029/2019GB006239, 2019.

660 Ross, O. N., Frayse, M., Pinazo, C. and Pairaud, I.: Impact of an intrusion by the Northern Current on the
661 biogeochemistry in the eastern Gulf of Lion, NW Mediterranean, *Estuar. Coast. Shelf Sci.*, 170, 1–9,
662 doi:10.1016/j.ecss.2015.12.022, 2016.

663 Rykiel, E. J.: Testing ecological models: The meaning of validation, *Ecol. Modell.*, 90(3), 229–244, doi:10.1016/0304-
664 3800(95)00152-2, 1996.

665 Sarthou, G., Timmermans, K. R., Blain, S. and Tréguer, P.: Growth physiology and fate of diatoms in the ocean: a
666 review, *J. Sea Res.*, 53(1), 25–42, doi:10.1016/j.seares.2004.01.007, 2005.

667 Schneider, A., Wallace, D. W. R. and Körtzinger, A.: Alkalinity of the Mediterranean Sea, *Geophys. Res. Lett.*, 34(15),
668 doi:10.1029/2006GL028842, 2007.

669 Sempéré, R., Charrière, B., van Wambeke, F., and Cauwet, G.: Carbon inputs of the Rhône River to the Mediterranean
670 Sea: Biogeochemical implications, *Global Biogeochem. Cycles*, 14(2), 669–681, doi:10.1029/1999GB900069, 2000.

671 Small, C. and Nicholls, R. J.: A global analysis of human settlement in coastal zones, *J. Coast. Res.*, 19(3), 584–599
672 [online] Available from: <http://www.jstor.org/stable/4299200>, 2003.

673 Smith, C. L. and Tett, P.: A depth-resolving numerical model of physically forced microbiology at the European shelf
674 edge, *J. Mar. Syst.*, 26(1), 1–36, doi:10.1016/S0924-7963(00)00010-5, 2000.

675 Soetaert, K., Hofmann, A. F., Middelburg, J. J., Meysman, F. J. R. and Greenwood, J.: The effect of biogeochemical
676 processes on pH, *Mar. Chem.*, 105(1–2), 30–51, doi:10.1016/j.marchem.2006.12.012, 2007.

677 Tett, P.: A three-layer vertical and microbiological processes model for shelf seas., 1990.

678 Tett, P., Droop, M. R. and Heaney, S. I.: The Redfield ratio and phytoplankton growth rate, *J. Mar. Biol. Assoc. United*
679 *Kingdom*, 65(2), 487–504, doi:10.1017/S0025315400050566, 1985.

680 Thingstad, T. F.: Utilization of N, P, and organic C by heterotrophic bacteria . I. Outline of a chemostat theory with a
681 consistent concept of “maintenance” metabolism, *Mar. Ecol. Prog. Ser.*, 35, 99–109, doi:10.3354/meps035099, 1987.

682 Upström, L. R.: The boron/chlorinity ratio of deep-sea water from the Pacific Ocean, *Deep Sea Res. Oceanogr. Abstr.*,
683 21(2), 161–162, doi:10.1016/0011-7471(74)90074-6, 1974.

684 Upstill-Goddard, R. C.: Air-sea gas exchange in the coastal zone, *Estuar. Coast. Shelf Sci.*, 70(3), 388–404,
685 doi:10.1016/j.ecss.2006.05.043, 2006.

686 Wanninkhof, R. H.: Relationship between wind speed and gas exchange, *J. Geophys. Res.*, 97(C5), 7373–7382, 1992.

687 Weiss, R. F.: Carbon dioxide in water and seawater: the solubility of a non-ideal gas, *Mar. Chem.*, 2(3), 203–215,
688 doi:10.1016/0304-4203(74)90015-2, 1974.

689 Willmott, C. J.: Some comments on the evaluation of model performance, *Bull. Am. Meteorol. Soc.*, 63(11), 1982.

690 Wimart-Rousseau, C., Lajaunie-Salla, K., Marrec, P., Wagener, T., Raimbault, P., Lagadec, V., Lafont, M., Garcia,
691 N., Diaz, F., Pinazo, C., Yohia, C., Garcia, F., Xueref-Remy, I., Blanc, P. E., Armengaud, A. and Lefèvre, D.: Temporal
692 variability of the carbonate system and air-sea CO₂ exchanges in a Mediterranean human-impacted coastal site, *Estuar.*
693 *Coast. Shelf Sci.*, 236(February), doi:10.1016/j.ecss.2020.106641, 2020.

694 Xueref-Remy, I., Milne, M., Zoghbi, N., Yohia, C., Armengaud, A., Blanc, P.-E., Delmotte, M., Piazzola, J., Nathan,
695 B., Ramonet, M. and Lac, C.: Assessing atmospheric CO₂ variability in the Aix-Marseille metropolis area (France)
696 and its coastal Mediterranean Sea at different time scales within the AMC project, Prague, Aus, [online] Available
697 from: https://conference.icos-ri.eu/wp-content/uploads/2018/09/ICOS2018SC_Book_of_Abstracts.pdf, 2018a.

698 Xueref-Remy, I., Dieudonné, E., Vuillemin, C., Lopez, M., Lac, C., Schmidt, M., Delmotte, M., Chevallier, F., Ravetta,
699 F., Perrussel, O., Ciais, P., Bréon, F., Broquet, G., Ramonet, M. and Ampe, C.: Diurnal , synoptic and seasonal
700 variability of atmospheric CO₂ in the Paris megacity area, *Atmos. Chem. Phys.*, 18, 3335–3362, doi:10.5194/acp-18-
701 3335-2018, 2018b.

702 Yohia, C.: Genèse du mistral par interaction barocline et advection du tourbillon potentiel, *Climatologie*, 13, 24–37
703 [online] Available from: <https://doi.org/10.4267/climatologie.1182>, 2017.

704 Zappa, C. J., Raymond, P. A., Terray, E. A. and McGillis, W. R.: Variation in surface turbulence and the gas transfer
705 velocity over a tidal cycle in a macro-tidal estuary, *Estuaries*, 26(6), 1401–1415, 2003.
706
707

	Temperature	Wind	River input	Atmospheric CO ₂
S0 – Reference	In situ data of 2017	WRF model 2017	No	CAV station 2017
S1 - T increases	In situ data of 2017 +1.5°C	WRF model 2017	No	CAV station 2017
S2 - Wind constant	In situ data of 2017	7 m s ⁻¹	No	CAV station 2017
S3 - Wind events	In situ data of 2017	3 days at 20 m s ⁻¹	No	CAV station 2017
S4 - NO₃	In situ data of 2017	WRF model 2017	Yes, NO ₃	CAV station 2017
S5 - Non-urban	In situ data of 2017	WRF model 2017	No	OHP station 2017

709 Table 1: Forcing of the different scenarios (S) simulated with the model. See section 2.4 for details of scenarios.

710

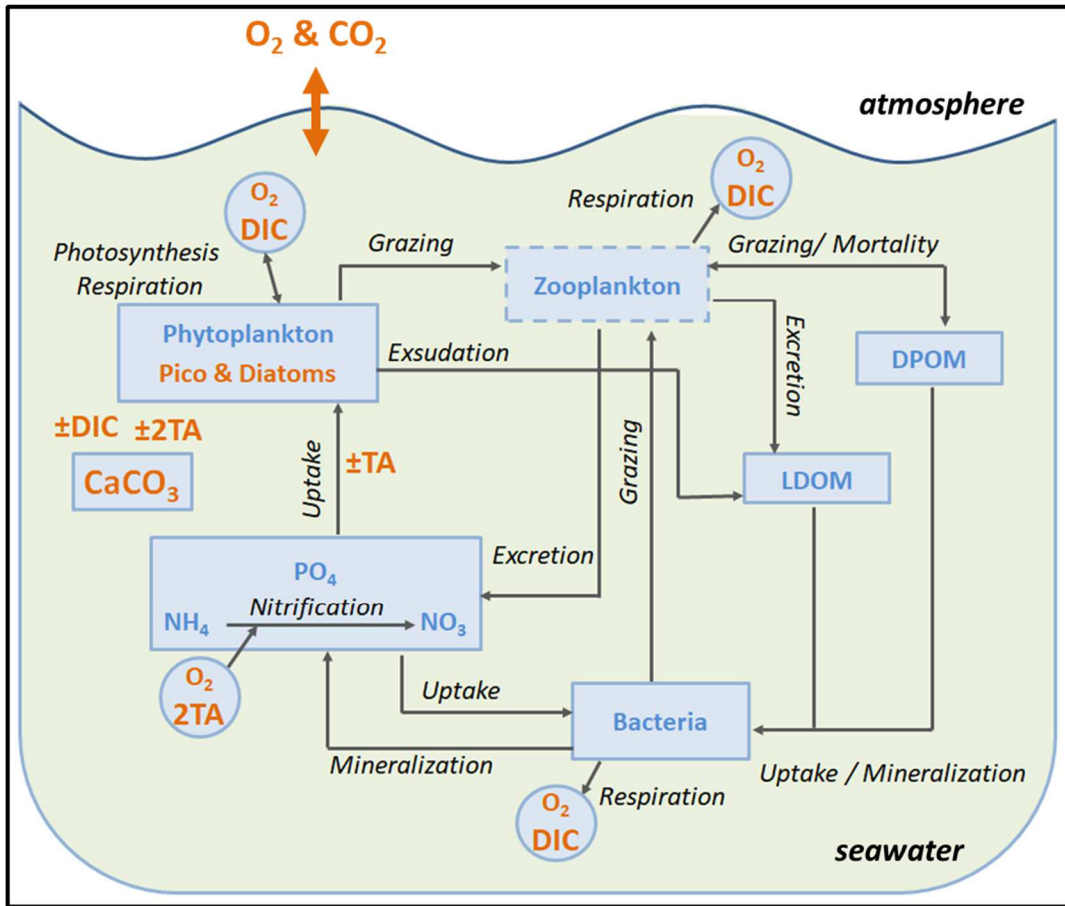
	Chl	seawater pCO ₂	pH	DIC	TA
Obs min-max	[0.10– 1.71]	[358 – 471]	[8.014 – 8.114]	[2260 – 2348]	[2561 – 2624]
Mod min-max	[0.03 – 0.73]	[331 – 522]	[7.979 – 8.171]	[2220 – 2323]	[2560– 2572]
Bias	-0.22	22.47	-0.016	-8.48	-24.91
WSS	0.36	0.69*	0.75*	0.71*	0.43
N	22	20	21	20	20

711 Table 2: Statistical evaluation of observations vs. model for 2017 year: observed and simulated minimum and maximum
712 values, WSS = Wilmott Skill Score, N = number of measurements. Units of bias are those of modeled variables: chlorophyll
713 *a* (Chl, mg m⁻³), seawater pressure of CO₂ (seawater pCO₂, µatm), pH, dissolved inorganic carbon (DIC, µmol kg⁻¹) and total
714 alkalinity (TA, µmol kg⁻¹). *significant value of WSS (> 0.70).

715

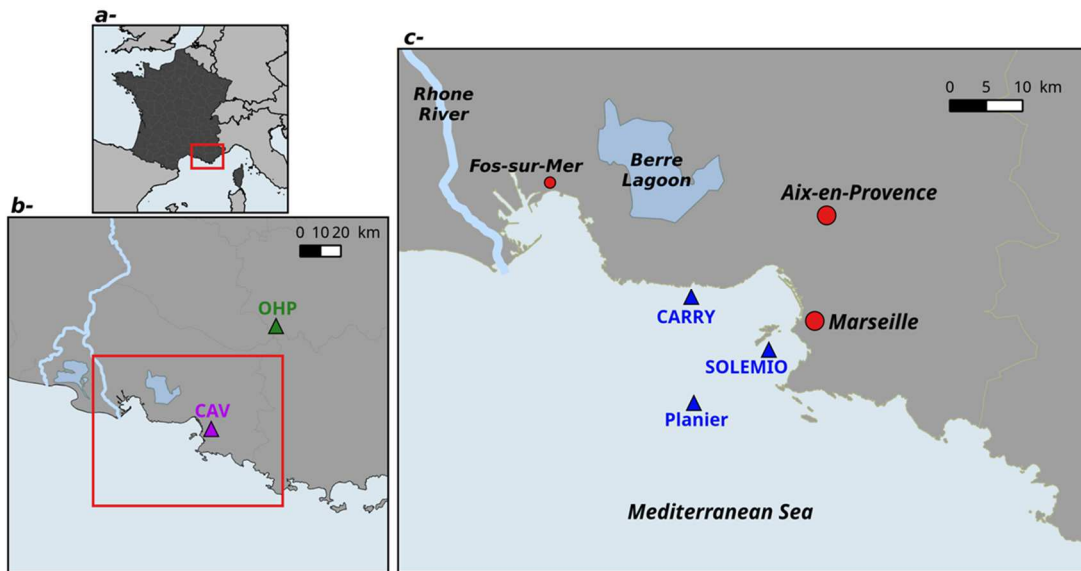
		Aeration	GPP	R _A	R _H	R	NEP
Year		0.017	-0.413	0.065	0.348	0.413	0
Mean flux	MWC	-0.245	-0.314	0.052	0.176	0.228	0.086
	SWC	0.405	-0.521	0.079	0.555	0.634	-0.113
Contribution	Year	78%	11%	2%	9%	11%	-

716 Table 3: Mean flux values (mmol m⁻³ d⁻¹) and the contribution of each process to the DIC variations for the reference
717 simulation over the year and SWC/MWC periods. GPP: Gross primary production, R_A: Autotroph respiration, R_H:
718 heterotroph respiration, NEP: Net Ecosystem Production



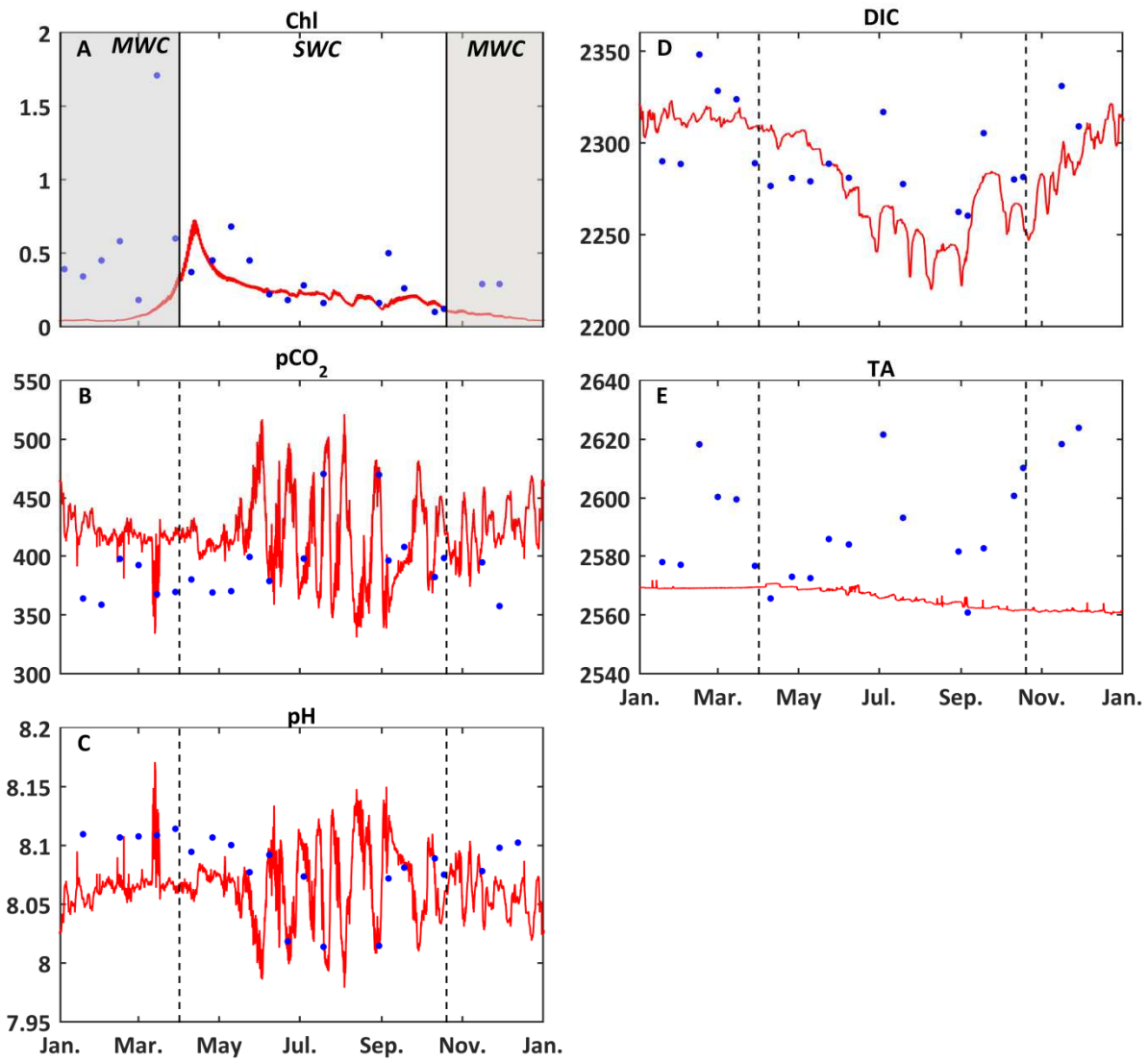
720
721
722
723
724
725
726
727

Figure 1: Schematic diagram of the biogeochemical model Eco3M-CarbOx. Explicit state variables of the model are indicated in continuous-line box or circles except the implicit variable for zooplankton (dotted line box). Orange-written state variables are added variables compared to the preexisting biogeochemical model of Fraysse et al. (2013). Arrows represent processes between two state variables. TA: Total Alkalinity. DIC: Dissolved Inorganic Carbon, CO₂: carbon dioxide, O₂: Oxygen, CaCO₃: calcium carbonate.



728
 729 **Figure 2: Map of study area: The Region Sud (A), Aix-Marseille Metropolis (B), the Bay of Marseille (C). CAV= Cinq**
 730 **A Venues Station (urban site), OHP: Observatoire de Haute Provence station (non-urban site), Carry, Solemio, Planier:**
 731 **Marine study sites in the Bay of Marseille.**

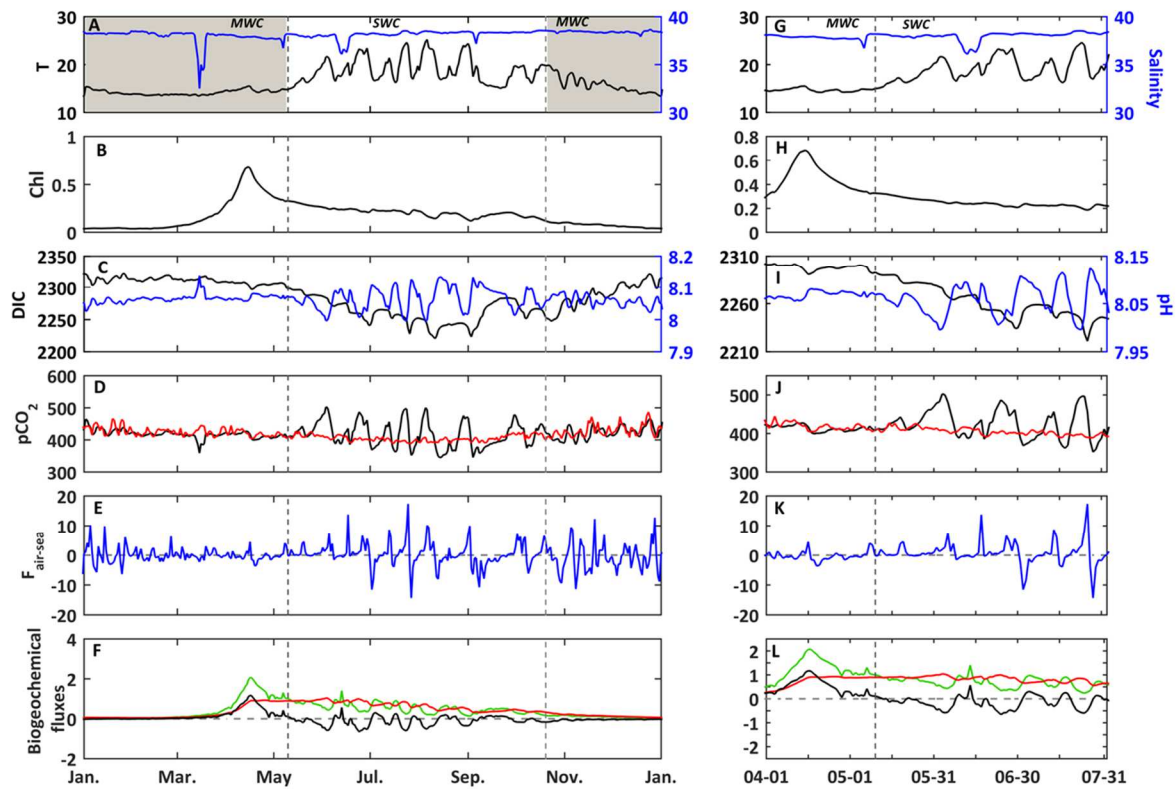
732



734
735
736
737
738

Figure 3: Comparison of model results (red) and *in situ* data (blue) at the surface of the SOLEMIO station. (A) Chlorophyll-*a* concentrations (mg m⁻³), (B) pCO₂ (µatm), (C) pH, (D) DIC (µmol kg⁻¹), (E) TA (µmol kg⁻¹). The value of each state variable represents the mean around ±5 days of the sampling date. The shaded area and dotted black line delimit the SWC and MWC periods.

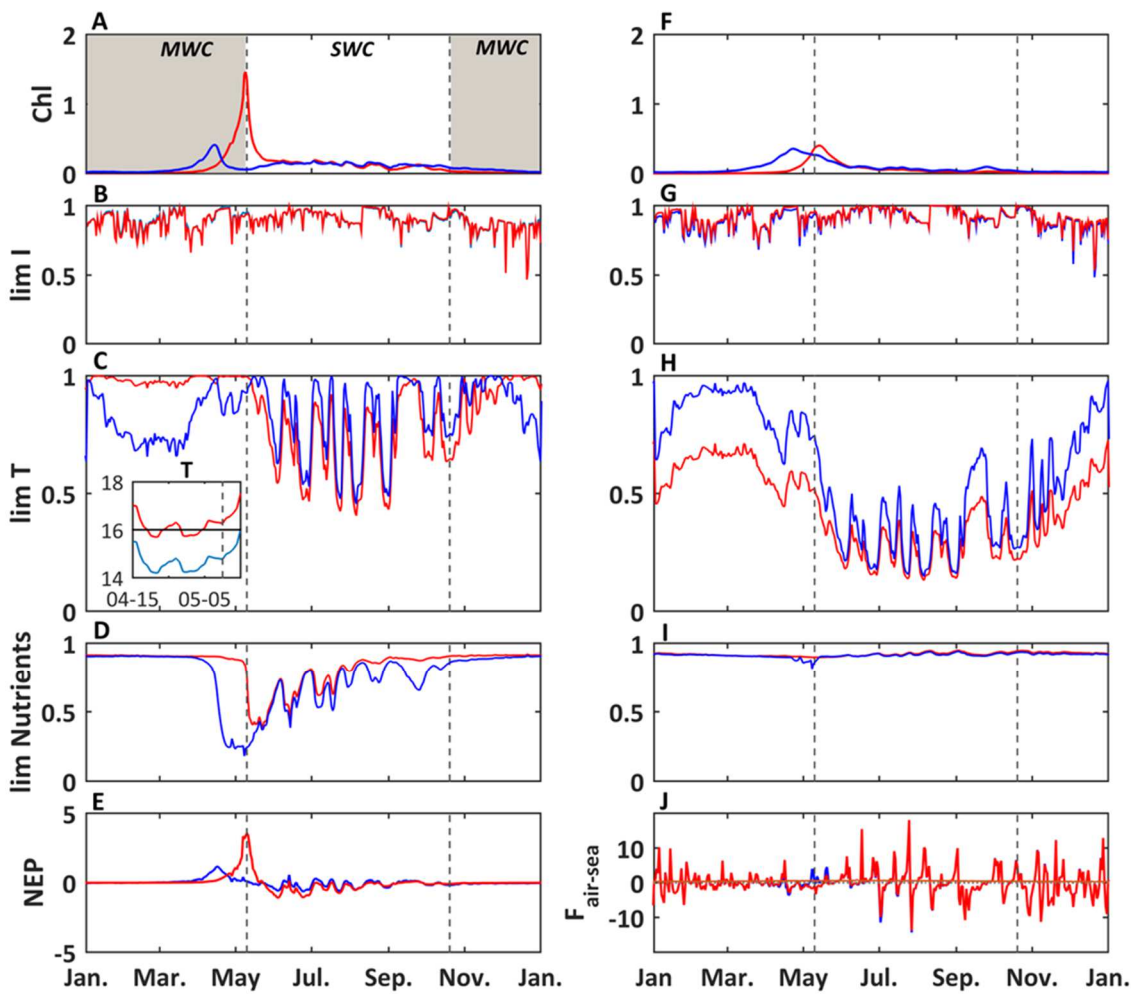
739



740
741
742
743
744
745
746
747

Figure 4: In the left panels: year 2017, right panels: temporal focus between April 1st and July 31th, 2017. *In situ* daily average of (A, G) temperature (°C, black line) and salinity (blue line) at the SOLEMIO station (at the surface). Modeled daily average (B, H) chlorophyll *a* concentrations (mg m^{-3} , black line) (C, I) DIC ($\mu\text{mol kg}^{-1}$, black line) and pH (blue line), (D, J) seawater $p\text{CO}_2$ (μatm , black line) and atmosphere $p\text{CO}_2$ from OHP (μatm , red line), (E, K) air-sea CO_2 fluxes $\text{mmol m}^{-3} \text{d}^{-1}$, (F, L) Gross Primary Production ($\text{mmol m}^{-3} \text{d}^{-1}$, green line), total respiration ($\text{mmol m}^{-3} \text{d}^{-1}$, red line) and Net Ecosystem Production ($\text{mmol m}^{-3} \text{d}^{-1}$, black line). The shaded areas and dotted black lines delimit the SWC and MWC periods.

748



750

751

752

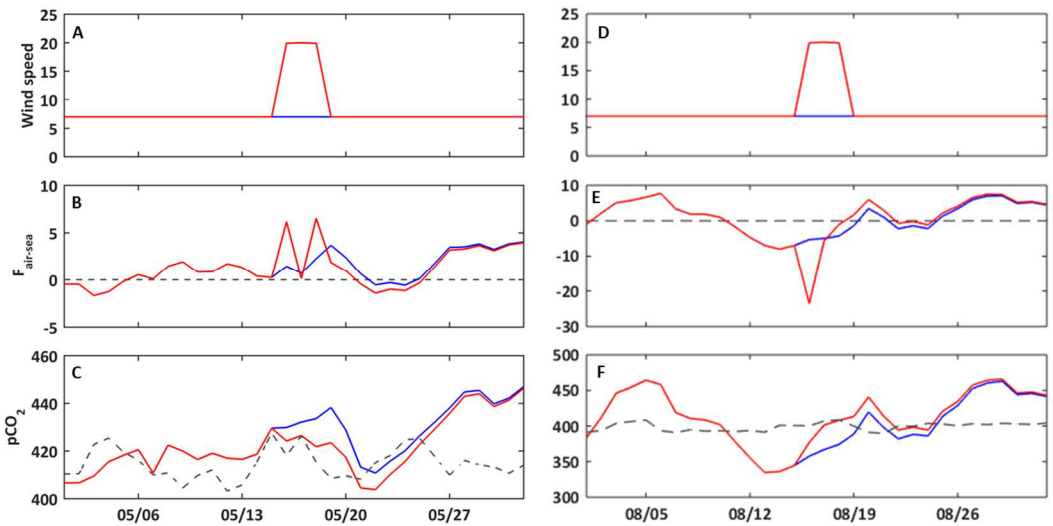
753

754

755

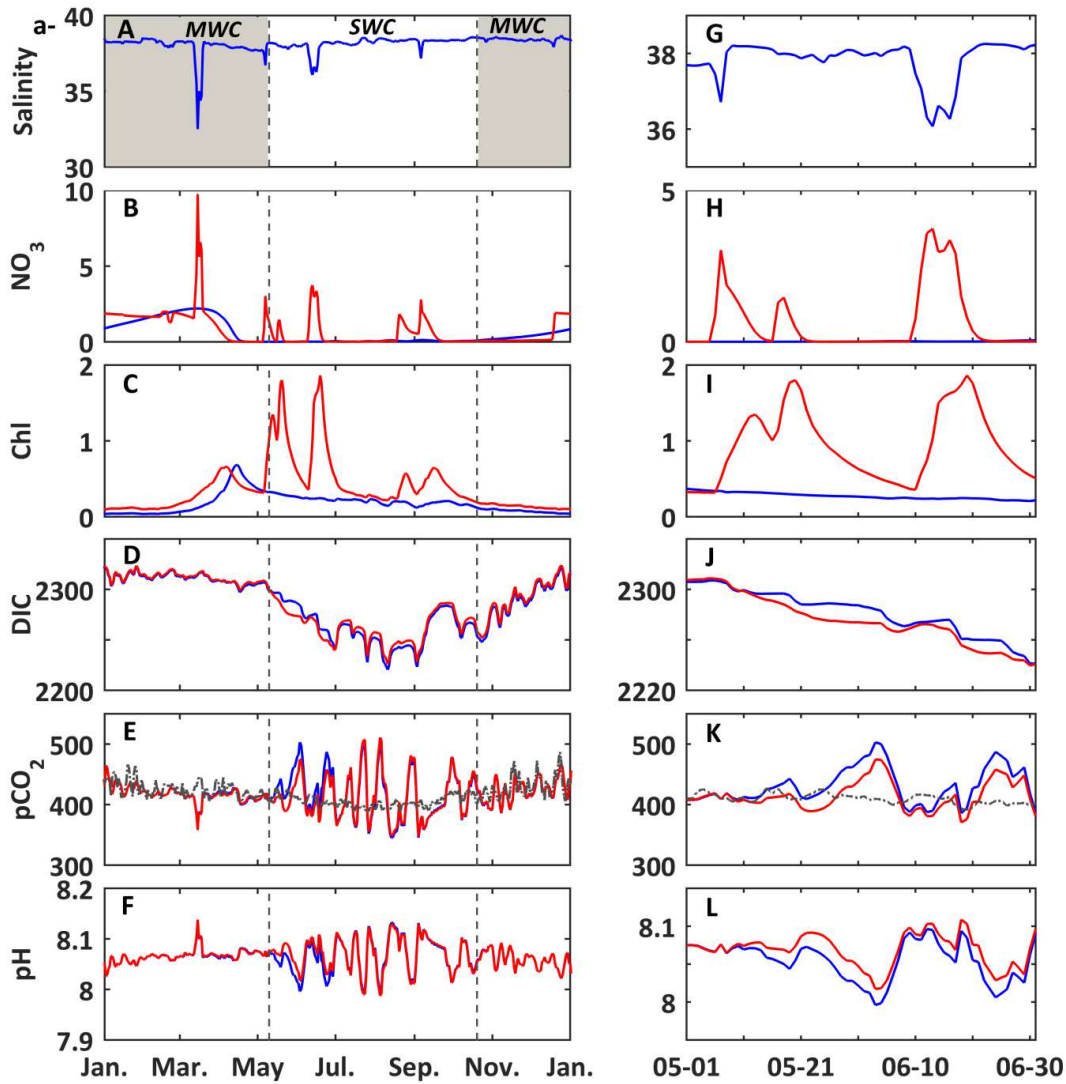
Figure 5: Modeled daily average chlorophyll *a* concentrations (mg m^{-3}) (A), light limitation (B), temperature limitation, and a zoom from April 15th to May 5th of temperature (C) and nutrient limitation (D) for picophytoplankton and the same set for diatoms (F, G, H and I). Modeled daily average NEP ($\text{mmol m}^{-3} \text{d}^{-1}$, E) and air-sea CO_2 flux ($\text{mmol m}^{-3} \text{d}^{-1}$, J). Reference simulation (S0, blue line) and temperature-shifted simulation by 1.5°C (S2, red line). The shaded area and dotted black lines delimit the SWC and MWC periods.

756



757
 758 **Figure 6: Temporal evolution for May (left panels) and August (right panels) 2017 of the wind speed (m s^{-1} , A, D); air-sea**
 759 **CO_2 fluxes ($\text{mmol m}^{-3} \text{d}^{-1}$, B, E); seawater partial pressure of CO_2 (μatm , C, F). Constant wind scenario (S2, blue line) and**
 760 **wind event scenario (S3, red line). On panels C and F, the dashed line represents the atmosphere partial pressure of CO_2**
 761 **(μatm) at the CAV station.**

762

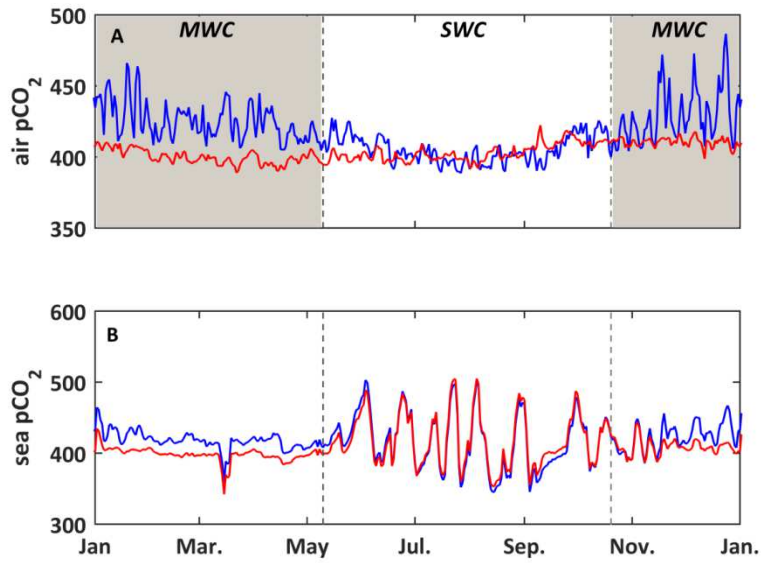


763
764
765
766
767
768

Figure 7: In the left panels: year 2017 and right panels: temporal focus between May 1st and July 1st, 2017. (A, G) *In situ* daily average of salinity. Modeled daily average (B, H) nitrate concentrations (mmol m^{-3}); (C, I) chlorophyll *a* concentrations (mg m^{-3}); (D, J) DIC ($\mu\text{mol kg}^{-1}$); (E, K) seawater $p\text{CO}_2$ (μatm), and (F, L) $p\text{H}$. Reference simulation (S0, blue line) and nitrate supply simulation (S4, red line). On panels E and K, the dashed line represents the atmosphere partial pressure of CO_2 (μatm) at the CAV station. The shaded area and dotted black lines delimit the SWC and MWC periods.

769

770
771



772
773
774
775
776
777

Figure 8: (A) Temporal evolution for the year 2017 of the observed partial pressure of CO₂ (μatm) in the atmosphere at the CAV station, called the “urban scenario” (S0, blue line), and at the OHP station, called the “non-urban scenario”, and in seawater (S6, red line). (B) Temporal evolution for the year 2017 of the modeled seawater partial pressure of CO₂ (μatm) with forcings from the urban (S0, blue line) and non-urban (S6, red line) scenarios. The shaded area and dotted black lines delimit the SWC and MWC periods.

Appendix A: Details of resolution of carbonate system module

A.1. Calculation of carbonate systems constants:

- 780 • Total Fluoride (TF) concentrations from Riley (1965) in mol kg⁻¹:

$$TF = \frac{0.000067}{18.998} \cdot \frac{S}{1.80655}$$

- Total Sulphate (TS) concentration from Morris and Riley (1966) in mol kg⁻¹:

$$TS = \frac{0.14}{96.062} \cdot \frac{S}{1.80655}$$

- Calcium ion concentration from Riley and Tongudai (1967) in mol kg⁻¹:

785 $Ca^{2+} = \frac{0.02128}{40.087} \cdot \frac{S}{1.80655}$

- Total Boron (TB) concentration from Uppström (1974) in mol kg⁻¹:

$$TB = \frac{0.000416 \cdot S}{35}$$

- Ionic Strength (IonS) from Millero (1982):

$$IonS = \frac{19.924 \cdot S}{1000 - 1.005 \cdot S}$$

790

The constants are calculated on the total pH scale except for K_S on free pH scale

- If necessary, pH scale conversion factors are following:

From Seawater pH Scale (SWS) to total pH scale: $SWStoTOT = \frac{1 + \frac{TS}{K_S}}{1 + \frac{TS}{K_S} + \frac{TF}{K_F}}$

From Free pH Scale to Total pH scale: $FREEtoTOT = 1 + \frac{TS}{K_S}$

795

- K_S equilibrium constant of dissociation of HSO_4^- from Dickson (1990a) in mol kg⁻¹:

$$K_S = \frac{-4276.1}{T_{(K)}} + 141.328 - 23.093 \cdot \log(T_{(K)}) + \left(324.57 - 47.986 \cdot \log(T_{(K)}) - \frac{13856}{T_{(K)}} \right) \cdot Ions^2$$

$$K_S = K_S + \left(-771.54 + 114.723 \cdot \log(T_{(K)}) + \frac{35474}{T_{(K)}} \right) \cdot Ions + \frac{-2698}{T_{(K)}} \cdot Ions^{\frac{3}{2}} + \frac{1776}{T_{(K)}} \cdot Ions^2$$

$$K_S = e^{K_S} \cdot (1 - 0.001005 \cdot S)$$

- 800 • K_F equilibrium constant of dissociation of hydrogen fluoride (HF) formation from Dickson and Riley (1979) in mol kg⁻¹:

$$K_F = e^{\frac{1590.2}{T_{(K)}} - 12.641 + 1.525 \cdot Ions^{\frac{1}{2}}} \cdot (1 - 0.001005 \cdot S)$$

- K_B equilibrium constant of dissociation of boric acid from Dickson (1990b) in mol kg⁻¹

$$K_B = (-8966.9 - 2890.53 \cdot S^{\frac{1}{2}} - 77.942 \cdot S + 1.728 \cdot S^{\frac{3}{2}} - 0.0996 \cdot S^2) / T_{(K)}$$

$$K_B = K_B + 148.0248 + 137.1942 \cdot S^{\frac{1}{2}} + 1.62142 \cdot S + (-24.4344 - 25.085 \cdot S^{\frac{1}{2}} - 0.2474 \cdot S) \cdot \log(T) + 0.053105$$

805 $\cdot S^{\frac{1}{2}} \cdot T$

- K_0 constant of CO₂ solubility from Weiss (1974) in mol kg⁻¹ atm⁻¹:

$$K_0 = \exp\left(-60.2409 + 93.4517 \cdot \frac{100}{T(K)} + 23.3585 \cdot \log\left(\frac{T(K)}{100}\right) + S \cdot \left(0.023517 - 0.023656 \cdot \frac{T(K)}{100} + 0.0047036 \cdot \left(\frac{T(K)}{100}\right)^2\right)\right)$$

- K_e : Dissociation constant of water from Millero (1995) in (mol kg⁻¹)²:

$$K_e = \exp\left(\frac{-13847.26}{T(K)} + 148.9802 - 23.6521 \cdot \log(T(K)) + \left(-5.977 + \frac{118.67}{T(K)} + 1.0495 \cdot \log(T(K))\right) \cdot S^{\frac{1}{2}} - 0.01615 \cdot S\right)$$

810 $K_e = K_e \cdot SWStoTOT$, on total pH scale in mol kg⁻¹

- K_1 and K_2 from Lueker et al. (2000) in mol kg⁻¹:

$$K_1 = 10^{\frac{-3633.86}{T(K)} + 61.2172 - 9.6777 \cdot \log(T(K)) + 0.011555 \cdot S - 0.0001152 \cdot S^2}$$

$$K_2 = 10^{\frac{-471.78}{T(K)} + 251.929 - 3.16967 \cdot \log(T(K)) + 0.01781 \cdot S - 0.0001122 \cdot S^2}$$

- K_{ca} for calcite from Mucci (1983) in (mol kg⁻¹)²:

815 $K_{ca} = 10^{\frac{-171.9065 - 0.077993 \cdot T(K) + \frac{2839.319}{T(K)} + 71.595 \cdot \log_{10}(T(K)) + (-0.77712 + 0.0028426 \cdot T(K) + \frac{178.34}{T(K)} \cdot S^{\frac{1}{2}} - 0.07711 \cdot S + 0.0041249 \cdot S^{\frac{3}{2}}}{1}}$

- All the constants are corrected by the effect of hydrostatic pressure:

$$R = 83.1451 \text{ in ml bar}^{-1} \text{ K}^{-1} \text{ mol}^{-1}$$

$$\ln K_1 fac = \frac{\left(25.5 - 0.1271 \cdot T(^{\circ}C) + 0.5 \cdot \left(\frac{-3.08 + 0.0877 \cdot T(^{\circ}C)}{1000}\right) \cdot P_{bar}\right) \cdot P_{bar}}{R \cdot T(K)}; K_1 = K_1 \cdot e^{\ln K_1 fac}$$

$$\ln K_2 fac = \frac{\left(15.82 - 0.0219 \cdot T(^{\circ}C) + 0.5 \cdot \left(\frac{1.13 + 0.1475 \cdot T(^{\circ}C)}{1000}\right) \cdot P_{bar}\right) \cdot P_{bar}}{R \cdot T(K)}; K_2 = K_2 \cdot e^{\ln K_2 fac}$$

820 $\ln K_B fac = \frac{\left(29.48 - 0.1622 \cdot T(^{\circ}C) + 0.002608 \cdot T(^{\circ}C)^2 + 0.5 \cdot \left(\frac{-2.84}{1000}\right) \cdot P_{bar}\right) \cdot P_{bar}}{R \cdot T(K)}; K_B = K_B \cdot e^{\ln K_B fac}$

$$\ln K_e fac = \frac{\left(20.02 - 0.1119 \cdot T(^{\circ}C) + 0.001409 \cdot T(^{\circ}C)^2 + 0.5 \cdot \left(\frac{-5.13 + 0.0794 \cdot T(^{\circ}C)}{1000}\right) \cdot P_{bar}\right) \cdot P_{bar}}{R \cdot T(K)}; K_e = K_e \cdot e^{\ln K_e fac}$$

$$\ln K_F fac = \frac{\left(9.78 - 0.009 \cdot T(^{\circ}C) + 0.0009429 \cdot T(^{\circ}C)^2 + 0.5 \cdot \left(\frac{-3.91 + 0.054 \cdot T(^{\circ}C)}{1000}\right) \cdot P_{bar}\right) \cdot P_{bar}}{R \cdot T(K)}; K_F = K_F \cdot e^{\ln K_F fac}$$

$$\ln K_S fac = \frac{\left(18.03 - 0.0466 \cdot T(^{\circ}C) + 0.000316 \cdot T(^{\circ}C)^2 + 0.5 \cdot \left(\frac{-4.53 + 0.009 \cdot T(^{\circ}C)}{1000}\right) \cdot P_{bar}\right) \cdot P_{bar}}{R \cdot T(K)}; K_S = K_S \cdot e^{\ln K_S fac}$$

$$\ln K_{ca} fac = \frac{\left(48.76 - 0.5304 \cdot T(^{\circ}C) + 0.5 \cdot \left(\frac{-11.76 + 0.3692 \cdot T(^{\circ}C)}{1000}\right) \cdot P_{bar}\right) \cdot P_{bar}}{R \cdot T(K)}; K_{ca} = K_{ca} \cdot e^{\ln K_{ca} fac}$$

- 825 • Calculation of the Fugacity factor:

We suppose that the pressure is at one atmosphere or close to it (Weiss, 1974):

$$P_{atm} = 1.01325 \text{ bar}$$

$$\delta = 57.7 - 0.118 \cdot T \text{ in cm}^3 \text{ mol}^{-1}$$

$$b = -1636.75 + 12.0408 \cdot T - 0.0327957 \cdot T^2 + 3.16528 \cdot 0.00001 \cdot T^3 \text{ in cm}^3 \text{ mol}^{-1}$$

830 $FugFac = \exp\left(\frac{(b + 2 \cdot \delta) \cdot P_{atm}}{R \cdot T}\right)$

A.2. Resolution of carbonate system

To resolve the carbonate system, we calculate the δpH , which is the difference of pH between two iterations of the model. We initialize the run by imposing a pH value of 8.

```

835  if (nbiter < 1) pH = 8
      pHtol = 0.001 ! tolerance for iterations end
      deltaph = pHtol + 1
      do while (abs(deltaph) > 0.0001)
        H = 10-pH
        Denom = H2 + K1 · H + K1 · K2
840    CAlk = DIC · K1 · ( $\frac{H + 2 \cdot K_2}{Denom}$ )
        BAlk =  $\frac{TB \cdot K_B}{K_B + H}$ 
        OH =  $\frac{K_e}{H}$ 
        FreetoTot = 1 +  $\frac{TS}{K_S}$ 
845    Hfree =  $\frac{H}{FreetoTot}$ 
        HSO4 =  $\frac{TS}{1 + \frac{K_S}{Hfree}}$ 
        HF =  $\frac{TF}{1 + \frac{K_F}{Hfree}}$ 
        Residual = TA - CAlk - BAlk - OH + Hfree + HSO4 + HF
        Slope = DIC · H · K1 · (H2 + K1 · K2 + 4 · H · K2)
850    Slope =  $\frac{Slope}{Denom^2} + OH + H + \frac{BAlk \cdot H}{K_B + H}$ 
        Slope = log10 · Slope
        deltaph = Residual/Slope ! this is Newton's method
        do while (abs(deltaph) > 1) deltaph =  $\frac{deltaph}{2}$  ! to keep the jump from being too big
      enddo
855  pH = pH + deltaph ! Is on the same scale as K1 and K2 were calculated, i.e. total pH scale
      pCO2 = ( $\frac{DIC \cdot H^2}{H^2 + K_1 \cdot H + K_1 \cdot K_2}$ ) ·  $\frac{10^6}{K_0 \cdot FugFac}$  ! in µatm
      CO2 =  $\frac{DIC \cdot 10^6}{1 + \frac{K_1}{H} + \frac{K_1 \cdot K_2}{H^2}}$ 
      HCO3 =  $\frac{K_1 \cdot CO_2}{H}$ 
      CO3 =  $\frac{K_2 \cdot HCO_3}{H}$ 
860  Omega =  $\frac{Ca \cdot CO_3 \cdot 10^{-6}}{K_{ca}}$ 

```

Appendix B: Biogeochemical model variables and parameters

Table B1: Initial conditions of the state variables of Eco3M-CarbOx model (*diagnostic variables)

Variables	Name	Unit	values
Picophytoplankton	<i>PicoC</i>	mmolC m ⁻³	0.0480
	<i>PicoN</i>	mmolN m ⁻³	0.0092
	<i>PicoP</i>	mmolP m ⁻³	0.0003
Diatom	<i>DiaC</i>	mmolC m ⁻³	0.0571
	<i>DiaN</i>	mmolN m ⁻³	0.0089
	<i>DiaP</i>	mmolP m ⁻³	0.0007
Bacteria	<i>BacC</i>	mmolC m ⁻³	0.1083
	<i>BacN</i>	mmolN m ⁻³	0.0379
	<i>BacP</i>	mmolP m ⁻³	0.0039
DPOM Detrital Particulate organic matter	<i>DPOC</i>	mmolC m ⁻³	0.1252
	<i>DPON</i>	mmolN m ⁻³	0.0307
	<i>DPOP</i>	mmolP m ⁻³	0.0021
LDOM Labile Dissolved organic matter	<i>LDOC</i>	mmolC m ⁻³	1.0990
	<i>LDON</i>	mmolN m ⁻³	8.7980
	<i>LDOP</i>	mmolP m ⁻³	0.0018
DIM Dissolved inorganic matter	NH ₄	mmolN m ⁻³	0.3375
	NO ₃	mmolN m ⁻³	0.6723
	PO ₄	mmolP m ⁻³	0.7150
	DO	mmolO m ⁻³	257.00
	DIC	μmolC kg ⁻¹	2358.4
Total alkalinity	TA	μmolC kg ⁻¹	2660.5
Sea water partial pressure of CO₂	<i>p</i> CO ₂	μatm	371.28
pH	<i>p</i> H	-	8.1099
calcium carbonate	CaCO ₃	mmol m ⁻³	1.0000
<i>Picophytoplankton chlorophyll*</i>	<i>PicoChl</i>	mgChl m ⁻³	0.0193
<i>Diatom chlorophyll*</i>	<i>DiaChl</i>	mgChl m ⁻³	0.0229
Number of bacteria*	NBA	10 ¹² cell m ⁻³	0.2000

Table B2: Balance equations of Eco3M-CarbOx model

Variables	Balance equation
Pico- phytoplankton	$\frac{\partial PicoC}{\partial t} = R_{PP}^{PicoC} - R_{resp}^{PicoC} - R_{exu}^{PicoC} - R_{Gr}$
	$\frac{\partial PicoN}{\partial t} = R_{uptPicoN}^{NH_4} + R_{uptPicoN}^{NO_3} - R_{exu}^{PicoN} - R_{Gr}$
	$\frac{\partial PicoP}{\partial t} = R_{uptPicoP}^{PO_4} - R_{exu}^{PicoP} - R_{Gr}$
	$PicoChl = Q_C^N \cdot (Q_{N,min}^{Chl} + f_Q \cdot (Q_{N,max}^{Chl} - Q_{N,min}^{Chl})) \cdot PicoC$
Diatom	$\frac{\partial DiaC}{\partial t} = R_{PP}^{DiaC} - R_{resp}^{DiaC} - R_{exu}^{DiaC} - R_{Gr}$
	$\frac{\partial DiaN}{\partial t} = R_{uptDian}^{NH_4} + R_{uptDian}^{NO_3} - R_{exu}^{DiaN} - R_{Gr}$
	$\frac{\partial DiaP}{\partial t} = R_{uptDiaP}^{PO_4} - R_{exu}^{DiaP} - R_{Gr}$
	$DiaChl = Q_C^N \cdot (Q_{N,min}^{Chl} + f_Q \cdot (Q_{N,max}^{Chl} - Q_{N,min}^{Chl})) \cdot DiaC$
Bacteria	$\frac{\partial BacC}{\partial t} = R_{uptBac}^{DPOC} + R_{uptBac}^{LDOC} - R_{BR} - R_{Gr}^{BacC}$
	$\frac{\partial BacN}{\partial t} = R_{uptBac}^{DPON} + R_{uptBac}^{LDON} + R_{uptBac}^{NH_4} - R_{miner}^{NH_4} - R_{Gr}^{BacN}$
	$\frac{\partial BacP}{\partial t} = R_{uptBac}^{DPOP} + R_{uptBac}^{LDOP} + R_{uptBac}^{PO_4} - R_{miner}^{PO_4} - R_{Gr}^{BacP}$
DPOM	$\frac{\partial DPOC}{\partial t} = R_{pf} + R_m - R_{Gr} - R_{uptBac}^{DPOC}$
	$\frac{\partial DPON}{\partial t} = R_{pf} + R_m - R_{Gr} - R_{uptBac}^{DPON}$
	$\frac{\partial DPOP}{\partial t} = R_{pf} + R_m - R_{Gr} - R_{uptBac}^{DPOP}$
LDOM	$\frac{\partial LDOC}{\partial t} = R_{exu}^{PicoC} + R_{exu}^{DiaC} + R_{exu}^{LDOC} - R_{uptBac}^{LDOC}$
	$\frac{\partial LDON}{\partial t} = R_{exu}^{PicoN} + R_{exu}^{DiaN} + R_{exu}^{LDON} - R_{uptBac}^{LDON}$
	$\frac{\partial LDOP}{\partial t} = R_{exu}^{PicoP} + R_{exu}^{DiaP} + R_{exu}^{LDOP} - R_{uptBac}^{LDOP}$
NH₄	$\frac{\partial NH_4}{\partial t} = R_{excr}^{NH_4} + R_{miner}^{NH_4} - R_{nit} - \sum R_{uptPhyN}^{NH_4} - R_{uptBac}^{NH_4}$
NO₃	$\frac{\partial NO_3}{\partial t} = R_{nit} - \sum R_{uptPhyN}^{NO_3}$
PO₄	$\frac{\partial PO_4}{\partial t} = R_{excr}^{PO_4} + R_{miner}^{PO_4} - \sum R_{uptPhyP}^{PO_4} - R_{uptBac}^{PO_4}$
DO	$\frac{\partial DO}{\partial t} = R_{aera} + \left(\frac{O}{C}\right) \cdot R_{PP}^{PhyC} + \left(\frac{O}{N}\right) \cdot R_{uptPhyN}^{NO_3} - \left(\frac{O}{C}\right) \cdot R_{resp}^{PhyC} - \left(\frac{O}{C}\right) \cdot R_{excr}^{DIC} - \left(\frac{O}{C}\right) \cdot R_{BR} - \left(\frac{O}{N}\right) \cdot R_{nit}$
DIC	$\frac{\partial DIC}{\partial t} = R_{aera} + R_{resp}^{PhyC} + R_{BR} + R_{excr}^{DIC} - R_{PP}^{PhyC} - R_{precip} + R_{diss}$
TA	$\frac{\partial TA}{\partial t} = 2 \cdot R_{diss} + (R_{uptPhyN}^{NO_3} + R_{uptPhyP}^{PO_4} - R_{uptPhyN}^{NH_4}) + R_{miner}^{NH_4} - 2 \cdot R_{precip} - 2 \cdot R_{nit}$

Table B3: Biogeochemical processes simulated by the Eco3M-CarbOx model

Notation	Biogeochemical processes	Unit	Formulation
R_{PP}^{Phy}	Primary production	$\text{molC m}^{-3} \text{ s}^{-1}$	$R_{PP}^{PhyC} = P_{max} \cdot f_T^{PP} \cdot f_I \cdot PhyC$
R_{res}^{Phy}	Phytoplankton respiration	$\text{molC m}^{-3} \text{ s}^{-1}$	$R_{res}^{PhyC} = k_r^{PhyC} \cdot PhyC$
$R_{uptPhy}^{NH_4}$	NH ₄ uptake by phytoplankton	$\text{molX m}^{-3} \text{ s}^{-1}$	$R_{uptPhyN}^{NH_4} = V_{N,max} \cdot \frac{NH_4}{NH_4 + K_{NH_4}}$
$R_{uptPhy}^{NO_3}$	NO ₃ uptake by phytoplankton	$\text{molN m}^{-3} \text{ s}^{-1}$	$R_{uptPhyN}^{NO_3} = V_{N,max} \cdot \frac{NO_3}{NO_3 + K_{NO_3}} \cdot \left(1 - \frac{I_{in} \cdot NH_4}{NH_4 + K_{in}}\right)$
$R_{uptPhy}^{PO_4}$	PO ₄ uptake by phytoplankton	$\text{molP m}^{-3} \text{ s}^{-1}$	$R_{uptPhyP}^{PO_4} = V_{P,max} \cdot \frac{PO_4}{PO_4 + K_{PO_4}}$
R_{exu}^{PhyC}	Phytoplankton exudation as LDOC	$\text{molC m}^{-3} \text{ s}^{-1}$	$R_{exu}^{PhyC} = (1 - f_Q) \cdot R_{PP}^{Phy}$
R_{exr}^{PhyX}	Phytoplankton exudation as LDON or LDOP	$\text{molX m}^{-3} \text{ s}^{-1}$	$R_{exu}^{PhyX} = (1 - h_Q^X) \cdot R_{uptX}^{Phy}$
R_{BP}	Bacterial production	$\text{cell m}^{-3} \text{ s}^{-1}$	$R_{BP} = \mu_{max}^{Ba} \cdot f_Q^{Ba} \cdot f_T^{Ba} \cdot NBA$
R_{BR}	Bacterial respiration	$\text{molC m}^{-3} \text{ s}^{-1}$	$R_{BR} = \rho_g^{Ba} \cdot Q_C^{Ba} \cdot R_{BP} + \rho_r^{Ba} \cdot (Q_C^{Ba} - Q_{C,min}^{Ba}) \cdot NBA$
R_{uptBac}^X	X uptake by bacteria	$\text{molX m}^{-3} \text{ s}^{-1}$	$R_{uptBac}^X = V_{max}^{BA} \cdot \frac{X}{X + K_X^{Ba}} \cdot f_T^{Ba} \cdot NBA$
R_{Gr}^{Phy}	Phytoplankton grazing by zooplankton	$\text{molX m}^{-3} \text{ s}^{-1}$	$R_{Gr}^{Phy} = g_{Phy} \cdot f_{Gr} \cdot Phy$
R_{Gr}^{DPOM}	DPOM grazing by zooplankton	$\text{molX m}^{-3} \text{ s}^{-1}$	$R_{Gr}^{DPOM} = g_{DPOM} \cdot f_{Gr} \cdot DPOM$

$$f_Q = \min[f_Q^N, f_Q^P]; f_Q^X = \frac{Q_C^X - Q_{C,min}^X}{Q_C^X - Q_{C,min}^X + \beta X}$$

$$f_T^{PP} = \max\left(\frac{2 \cdot (1-b) \cdot \frac{(T-T_{let})}{(T_{opt}-T_{let})}}{\left(\frac{(T-T_{let})}{(T_{opt}-T_{let})}\right)^2 - 2 \cdot b \cdot \frac{(T-T_{let})}{(T_{opt}-T_{let})} + 1}; 0\right)$$

$$f_I = \left[1 - \exp\left(\frac{-\alpha_{Chla} \cdot EPAR \cdot Q_C^{Chla}}{P_{max} \cdot f_Q \cdot f_T^{PP}}\right)\right]$$

$$V_{N,max} = Q_{C,max}^N \cdot R_{PP}^{Phy}$$

$$V_{P,max} = Q_{C,max}^P \cdot R_{PP}^{Phy}$$

$$h_Q^X = \frac{Q_{C,max}^X - Q_C^X}{Q_{C,max}^X - Q_{C,min}^X}$$

$$f_T^{Ba} = Q_{10} \frac{(T-T_{rem})}{10}$$

$$f_Q^{Ba} = \min\left[1 - \frac{Q_C^{Ba,min}}{Q_C^{Ba}}, 1 - \frac{Q_N^{Ba,min}}{Q_N^{Ba}}, 1 - \frac{Q_P^{Ba,min}}{Q_P^{Ba}}\right]$$

$$g_{DPOM} = \frac{g_{Pico} \cdot Pico + g_{Dia} \cdot Dia}{Pico + Dia};$$

$$f_{Gr} = \frac{DPOM}{Phy + DPOM}$$

R_{Gr}^{Bac}	Bacterial grazing by zooplankton	$\text{molX m}^{-3} \text{ s}^{-1}$	$R_{Gr}^{Ba} = R_{BP} \cdot \frac{Bac}{NBA}$	
R_{exc}^{DIM}	Zooplankton excretion as DIC, NH_4 and PO_4	$\text{molX m}^{-3} \text{ s}^{-1}$	$R_{exc}^{DIM} = \varepsilon_{DIM} \cdot d_X \cdot (1 - k_{X,zoo}) \cdot (R_{Gr}^{Phy} + R_{Gr}^{DPOM} + R_{Gr}^{Ba})$	
R_{exu}^{LDOM}	Zooplankton exudation as LDOM	$\text{molX m}^{-3} \text{ s}^{-1}$	$R_{exu}^{LDOM} = (1 - \varepsilon_{DIM}) \cdot d_X \cdot (1 - k_{X,zoo}) \cdot (R_{Gr}^{Phy} + R_{Gr}^{DPOM} + R_{Gr}^{Ba})$	
R_{pf}	Zooplankton egestion	$\text{molX m}^{-3} \text{ s}^{-1}$	$R_{pf} = (1 - d_X) \cdot (R_{Gr}^{Phy} + R_{Gr}^{DPOM} + R_{Gr}^{Ba})$	
R_m	Zooplankton mortality	$\text{molX m}^{-3} \text{ s}^{-1}$	$R_m = d_X \cdot k_{X,zoo} \cdot (R_{Gr}^{Phy} + R_{Gr}^{DPOM} + R_{Gr}^{Ba})$	
R_{miner}	Mineralization of organic matter by bacteria	$\text{molX m}^{-3} \text{ s}^{-1}$	$R_{miner}^X = (1 - h_Q^{Ba}) \cdot (R_{uptBac}^{LDOM} + R_{uptBac}^{DPOM} + R_{uptBac}^{DIM})$	
R_{nit}	Nitrification	$\text{molX m}^{-3} \text{ s}^{-1}$	$R_{nit} = k_{nit} \cdot f_T^{Ba} \cdot \frac{DO}{DO + K_{DO}} \cdot \text{NH}_4$	
R_{diss}	Carbonate dissolution	$\text{molC m}^{-3} \text{ s}^{-1}$	$R_{diss} = (1 - \Omega_C) \cdot k_{diss} \cdot [\text{CaCO}_3]$	$\Omega_C = \text{aragonite saturation}$
R_{precip}	Carbonate precipitation	$\text{molC m}^{-3} \text{ s}^{-1}$	$R_{precip} = k_{precip} \cdot \frac{(\Omega_C - 1)}{K_C + (\Omega_C - 1)} \cdot (R_{PP}^{Phy} - R_{resp}^{Phy})$	
R_{aera}	Gas exchange with atmosphere of DO or CO_2	$\text{molX m}^{-3} \text{ s}^{-1}$	$R_{aera} = \frac{k_{ex}}{H} \cdot ([DO]_{sea} - [DO]_{sat})$ $R_{aera} = \frac{k_{ex}}{H} \cdot \alpha \cdot (p\text{CO}_{2,sea} - p\text{CO}_{2,atm})$	$k_{ex} = 0.31 \cdot U_{10}^2 \cdot \frac{660^{0.5}}{Sc}$ H (depth), U_{10} (wind velocity) α (solubility), Sc (Schmidt number) and $[DO]_{sat}$ are function of T and S

Table B4: Value of parameters

Parameters		Pico	Dia	Unit	Reference
P_m^C	Maximal production	1.815	1.057	d ⁻¹	Sarthou et al. (2005)
m_1	Fraction of the solar energy flux photosynthetically available	0.43	0.43	-	Tett (1987)
m_2	Sea surface reflection	0.95	0.95	-	Tett (1987)
m_3	More rapid attenuation of polychromatic light near the sea surface	1.0	1.0	-	Tett (1987)
α_{Chla}	Chlorophyll-specific light absorption coefficient	8 10 ⁻⁶	5 10 ⁻⁶	m ² molC (gChla J) ⁻¹	Leblanc et al. (2018)
T_{opt}	Temperature optimal of growth	16.0	13.0	°C	-
T_{let}	Lethal temperature	11.0	9.0	°C	-
b	Shape factor for temperature curve	0.5	0.8	-	Lacroix and Grégoire (2002)
β_N	Coefficient in the quota function	0.0072	0.002	molN molC ⁻¹	Leblanc et al. (2018)
β_P	Coefficient in the quota function	0.0002	0.0005	molP molC ⁻¹	Leblanc et al. (2018)
$Q_{C,min}^N$	Minimum phytoplankton N:C ratio	0.115	0.07	molN molC ⁻¹	Leblanc et al. (2018)
$Q_{C,max}^N$	Maximum phytoplankton N:C ratio	0.229	0.18	molN molC ⁻¹	Leblanc et al. (2018)
$Q_{C,min}^P$	Minimum phytoplankton P:C ratio	0.0015	0.006	molP molC ⁻¹	Auger et al. (2011); Campbell et al. (2013)
$Q_{C,max}^P$	Maximum phytoplankton P:C ratio	0.0068	0.016	molP molC ⁻¹	Auger et al. (2011); Campbell et al. (2013)
$Q_{N,min}^{Chla}$	Minimum phytoplankton Chl:N ratio	1.0	1.0	gChl molN ⁻¹	Leblanc et al. (2018)**
$Q_{N,max}^{Chla}$	Maximum phytoplankton Chl:N ratio	2.2	2.7	gChl molN ⁻¹	Leblanc et al. (2018)
k_r^{PhyC}	Phytoplankton respiration rate	0.099	0.099	d ⁻¹	Faure et al. (2010)
K_{NO_3}	Half saturation constant for NO ₃	0.73	1.0	mmolN m ⁻³	Leblanc et al. (2018)
K_{NH_4}	Half saturation constant for NH ₄	0.07	0.015	mmolN m ⁻³	Leblanc et al. (2018)
K_{PO_4}	Half saturation constant for PO ₄	0.008	0.01	mmolP m ⁻³	Leblanc et al. (2018)**
I_{in}	Factor of inhibition	0.82	0.82	-	Harrison et al. (1996)
K_{in}	Amount of NH ₄ from which assimilation by NO ₃ is reduced.	0.578	0.578	mmolN m ⁻³	Harrison et al. (1996)
g	Grazing rate	1.452	0.846	d ⁻¹	Gutiérrez-Rodríguez et al. (2011)

** calibrated from parameter used in the cited article

Table B5: Value of parameters (continue)

Parameters		Value	Unit	Reference
NBA	Number of bacteria	0.20	10^{12} cell m^{-3}	Moran (2015)
μ_{max}^{Ba}	Bacterial production rate	8.36	d^{-1}	Fraysse et al. (2013)
$Q_{C,min}^{BA}$	Minimum bacteria C:cell ratio	0.49	$mmolC (10^{12} cell)^{-1}$	Fukuda et al. (1998)
$Q_{N,min}^{BA}$	Minimum bacteria N:cell ratio	0.09	$mmolN (10^{12} cell)^{-1}$	Fukuda et al. (1998)
$Q_{N,max}^{BA}$	Maximum bacteria N:cell ratio	0.23	$mmolN (10^{12} cell)^{-1}$	Fukuda et al. (1998)
$Q_{P,min}^{BA}$	Minimum bacteria P:cell ratio	0.005	$mmolP (10^{12} cell)^{-1}$	Fraysse et al. (2013)
$Q_{P,max}^{BA}$	Maximum bacteria P:cell ratio	0.02	$mmolP (10^{12} cell)^{-1}$	Fraysse et al. (2013)
ρ_g^{Ba}	Factor of carbon respired by bacteria	0.60	-	Thingstad (1987)
ρ_r^{Ba}	Respiration rate of bacteria	0.01	d^{-1}	Thingstad (1987)
$V_{DPOC,max}^{BA}$	Maximum DPOC uptake by bacteria	0.029	$mmolC (10^{12} cell)^{-1} d^{-1}$	Campbell et al. (2013)
$V_{LDOC,max}^{BA}$	Maximum LDOC uptake by bacteria	16.33	$mmolC (10^{12} cell)^{-1} d^{-1}$	Campbell et al. (2013)
$V_{DPON,max}^{BA}$	Maximum DPON uptake by bacteria	0.05	$mmolN (10^{12} cell)^{-1} d^{-1}$	Faure et al. (2010)
$V_{LDON,max}^{BA}$	Maximum LDON uptake by bacteria	0.32	$mmolN (10^{12} cell)^{-1} d^{-1}$	Faure et al. (2010)
$V_{NH_4,max}^{BA}$	Maximum NH_4 uptake by bacteria	0.32	$mmolN (10^{12} cell)^{-1} d^{-1}$	Faure et al. (2010)
$V_{DPOP,max}^{BA}$	Maximum DPOP uptake by bacteria	0.01	$mmolP (10^{12} cell)^{-1} d^{-1}$	Thingstad (1987)
$V_{LDOP,max}^{BA}$	Maximum LDOP uptake by bacteria	0.48	$mmolP (10^{12} cell)^{-1} d^{-1}$	Thingstad (1987)
$V_{PO_4,max}^{BA}$	Maximum PO_4 uptake by bacteria	0.48	$mmolP (10^{12} cell)^{-1} d^{-1}$	Thingstad (1987)
K_{DPOC}^{BA}	Half-saturation constant for DPOC	10.0	$mmolC m^{-3}$	Faure et al. (2010)
K_{LDOC}^{BA}	Half-saturation constant for LDOC	25.0	$mmolC m^{-3}$	-
K_{DPON}^{BA}	Half-saturation constant for DPON	0.50	$mmolN m^{-3}$	-
K_{LDON}^{BA}	Half-saturation constant for LDON	0.50	$mmolN m^{-3}$	-
$K_{NH_4}^{BA}$	Half-saturation constant for NH_4	0.15	$mmolN m^{-3}$	Leblanc et al. (2018)
K_{DPOP}^{BA}	Half-saturation constant for DPOP	0.08	$mmolP m^{-3}$	-
K_{LDOP}^{BA}	Half-saturation constant for LDOP	0.08	$mmolP m^{-3}$	Leblanc et al. (2018)
$K_{PO_4}^{BA}$	Half-saturation constant for PO_4	0.02	$mmolP m^{-3}$	Campbell et al. (2013)
ϵ_{DIC}	fraction excretion of DIC	0.31	-	Faure et al. (2010)
ϵ_{NH_4}	fraction excretion of NH_4	0.50	-	Faure et al. (2010)
ϵ_{PO_4}	Fraction excretion of PO_4	0.50	-	Fraysse et al. (2013)
d_C	Fraction of C assimilated	0.92	-	Gerber and Gerber (1979)
d_N	Fraction of N assimilated	0.95	-	Faure et al. (2010)
d_P	Fraction of P assimilated	0.95	-	Fraysse et al. (2013)
$k_{C,zoo}$	Net C growth efficiency	0.40	-	Gerber and Gerber (1979)
$k_{N,zoo}$	Net N growth efficiency	0.44	-	Le Borgne and Rodier (1997)
$k_{P,zoo}$	Net P growth efficiency	0.37	-	Le Borgne (1982)
Q_{10}	Temperature coefficient	2.0	-	-
T_{rem}	Reference temperature for mineralization	20.0	$^{\circ}C$	-
k_{nit}	Nitrification rate	0.05	d^{-1}	Lacroix and Grégoire (2002)
T_{nit}	Reference temperature for nitrification	10.0	$^{\circ}C$	-
K_{DO}	Half-saturation constant DO	30.0	$mmolO_2 m^{-3}$	Tett (1990)

k_{diss}	Dissolution rate	10.9	d^{-1}	Gehlen et al. (2007)
k_{precip}	Fraction of PIC to LPOC	0.02	-	Marty et al. (2002)
K_C	Half-saturation constant of $CaCO_3$ precipitation	0.40	$(\mu mol\ kg^{-1})^2$	
$\left(\frac{O}{C}\right)$	Ratio O:C	1.0	-	-
$\left(\frac{O}{N}\right)$	Ratio O:N	2.0	-	-

875

Appendix C: Short User Manual

After uploading the whole archive on the zenodo site (ref. doi: 10.5281/zenodo.3757677), the exact version of the Eco3M-CarbOx code used in this study can be run as following:

880 make !two executable files will be created : eco3M_ini.exe and eco3M.exe

- the file config.ini allows to define: the time, time step, and save time of simulation variables biogeochemical process
- Results files are stocked in "SORTIES" directory
- Boundary conditions and forcings data are stocked in "DATA" directory
- All subroutines of biogeochemical processes are stocked in "F_PROCESS" directory

885 For further information, please contact Dr. Frédéric DIAZ (frederic.diaz@univ-amu.fr) or Dr. Christel PINAZO (christel.pinazo@univ-amu.fr)